Monthly Notices of the ROYAL ASTRONOMICAL SOCIETY

MNRAS **531,** 2532–2550 (2024) https://doi.org/10.1093/mnras/stae1317
Advance Access publication 2024 May 23

Faraday rotation as a probe of radio galaxy environment in RMHD AGN jet simulations

L. A. Jerrim [1★] S. S. Shabala [1,2] P. M. Yates-Jones [1,2] M. G. H Krause [3] R. J. Turner [1] C. S. Anderson,[4] G. S. C. Stewart [1] C. Power [2,5] and P. E. Rodman [1,6]

[1]*School of Natural Sciences, University of Tasmania, Private Bag 37, Hobart TAS 7001, Australia*
[2]*ARC Centre of Excellence for All Sky Astrophysics in 3 Dimensions (ASTRO 3D), Australia*
[3]*Centre for Astrophysics Research, University of Hertfordshire, College Lane, Hatfield, Herts AL10 9AB, UK*
[4]*Research School of Astronomy and Astrophysics, The Australian National University, ACT 2611, Australia*
[5]*International Centre for Radio Astronomy Research, University of Western Australia, 35 Stirling Highway, Crawley, WA 6009, Australia*
[6]*Institute of Astronomy, University of Cambridge, Madingley Road, Cambridge CB3 0HA, UK*

Accepted 2024 May 20. Received 2024 May 18; in original form 2023 November 21

ABSTRACT

Active galactic nuclei (AGNs) play an integral role in galaxy formation and evolution by influencing galaxies and their environments through radio jet feedback. Historically, interpreting observations of radio galaxies and quantifying radio jet feedback has been challenging due to degeneracies between their physical parameters. In particular, it is well established that different combinations of jet kinetic power and environment density can yield indistinguishable radio continuum properties, including apparent size and Stokes I luminosity. We present an approach to breaking this degeneracy by probing the line-of-sight environment with Faraday rotation. We study this effect in simulations of three-dimensional relativistic magnetohydrodynamic AGN jets in idealized environments with turbulent magnetic fields. We generate synthetic Stokes I emission and Faraday rotation measure (RM) maps, which enable us to distinguish between our simulated sources. We find enhanced RMs near the jet head and lobe edges. We show that increasing the environment density and the average cluster magnetic field strength broadens the distribution of Faraday rotation measure values. We study the depolarization properties of our sources, finding that the hotspot regions depolarize at lower frequencies than the lobes. We quantify the effect of depolarization on the RM distribution, finding that the frequency at which the source is too depolarized to measure the RM distribution accurately is a probe of environmental properties. This technique offers a range of new opportunities for upcoming surveys, including probing radio galaxy environments and determining more accurate estimates of the AGN feedback budget.

Key words: MHD – galaxies: active – galaxies: jets – galaxies: magnetic fields – radio continuum: galaxies.

1 INTRODUCTION

Active galactic nuclei (AGNs) are the most energetic objects in the Universe and provide an important source of feedback in galaxy evolution (see review by Somerville & Davé 2015). AGN jets are the main source of AGN feedback in the local Universe (Fabian 2012). These jets act to heat and displace cool gas from cluster centres (McNamara & Nulsen 2007) and regulate star formation (Shabala, Kaviraj & Silk 2011; Nesvadba et al. 2021). These effects have been seen in both numerical (e.g. Sijacki et al. 2007; Vogelsberger et al. 2013) and semi-analytic (e.g. Granato et al. 2004; Raouf et al. 2017, 2019) galaxy formation models, as well as in numerical simulations of AGN jets (Gaibler et al. 2012; Yang & Reynolds 2016; Mandal et al. 2021).

To quantify the energetics of AGN feedback, an accurate measure of the kinetic power of radio jets is required; however, this cannot be directly inferred from the radio luminosity of the source. The size and luminosity of radio galaxies are influenced by both their intrinsic jet parameters and the ambient environment the jets interact with. Linear size–radio luminosity diagrams can be a useful tool to estimate jet power, age, and environmental properties if the relationship between these parameters is well known (Shklovskii 1963; Kaiser, Dennett-Thorpe & Alexander 1997; Turner & Shabala 2015; Hardcastle et al. 2019). Hardcastle & Krause (2013, 2014) have shown through numerical simulations that different combinations of jet and environment parameters can result in radio galaxies with similar radio luminosity and linear size. Therefore, the relationship between these parameters is not simple, and another constraint is required to make inferences about kinetic jet powers.

Polarimetry is a useful tool for studying AGN jets and has been used widely to study parsec-scale jets (e.g. Asada et al. 2002; Hovatta et al. 2012; Gabuzda, Nagle & Roche 2018) and kiloparsec-scale sources (e.g. Guidetti et al. 2011a; O'Sullivan et al. 2018; Sebokolodi et al. 2020). The polarization state of synchrotron emission from radio galaxies changes as the emission travels to the observer due to Faraday rotation (Ferriére, West & Jaffe 2021). The amount of

★ E-mail: larissa.jerrim@utas.edu.au

Faraday rotation is quantified by the rotation measure (RM) or the Faraday depth (ϕ) along the line of sight. For rotation by a foreground magnetized plasma, the Faraday depth is equal to the rotation measure (van Weeren et al. 2019). The polarization angle χ is given by (Burn 1966):

$$\chi = \chi_0 + \phi\lambda^2, \tag{1}$$

where χ_0 is the intrinsic polarization angle, ϕ is the Faraday depth, and λ is the wavelength of the emission. The Faraday depth depends on the magnetic field, cluster density, and the line of sight to the source as (Carilli & Taylor 2002)

$$\phi = 812 \int_0^l n_e \boldsymbol{B} \cdot \mathrm{d}\boldsymbol{l} \ \mathrm{rad/m^2}, \tag{2}$$

where the thermal electron number density n_e is in $\mathrm{cm^{-3}}$, the magnetic field strength $\boldsymbol{B}$ is in μG, and the path length $\mathrm{d}\boldsymbol{l}$ is in kpc. If RM $>$ 0, then on average, the magnetic field is directed towards the observer, and similarly, if RM $<$ 0, the magnetic field is directed away from the observer (as defined by Manchester 1972). Generally, there is a Galactic foreground RM contribution on the order of tens to a few hundred $\mathrm{rad/m^2}$ (Hutschenreuter et al. 2022).

If the foreground components of the RM can be removed, the residual RM of a radio galaxy can provide insights into the physics of the system. For example, O'Sullivan et al. (2018) presented RM observations of the radio galaxy PKS J0636-2036 and concluded that the dominant contributor to the RM of this radio galaxy is external Faraday depolarization due to either a magnetized intergalactic medium (IGM) or shock-enhanced IGM gas. Previously, Guidetti et al. (2011a) explored a model for RM observations of kiloparsec scale AGN jet lobes that incorporated both internal and external Faraday depolarization effects, finding that an amplified, swept-up IGM magnetic field can create band-like fluctuations in the RM. In observations, these bands may be hidden by foreground RM components that follow a Kolmogorov power spectrum.

This paper continues previous investigations into the RM properties of simulated AGN jets by Huarte-Espinosa, Krause & Alexander (2011a, b). Those authors performed three-dimensional (3D) magnetohydrodynamic (MHD) jet simulations with turbulent cluster magnetic fields and found that the compression of the intracluster medium (ICM), particularly by very light jets, enhances the RM. The enhancement is strongest towards the edge of the lobes and hence is expected to impact the statistics of the RM distribution. These studies represent some of the first works studying the RM in simulated AGN jets with magnetic fields evolved self-consistently with the jet, which we add to with this work.

We now aim to break the degeneracy between AGN jet and environment parameters using RMs. Our method uses the RM information for AGN jets as a proxy for the line-of-sight environment. Because the RM depends on the electron density and magnetic field along the line of sight, as shown in equation (2), the properties of the RMs are expected to differ between AGN jets in environments with different densities and magnetic fields. We test this method by simulating different combinations of jet and environment parameters and then comparing their radio observables and RM maps. We choose jet and environment parameters that closely resemble Cygnus A, as it is the archetypal powerful radio galaxy (Carilli & Barthel 1996). We also study the effect of the magnetic field structure size on our fiducial simulation.

The paper is structured as follows. In Section 2, we introduce the method and our simulation suite. We describe the implementation of the magnetic field in these simulations in Section 3. In Section 4.1, we present the dynamics of our simulations and in Section 4.2 we discuss the synthetic Stokes I emission of our simulated sources. We present the RM maps and distributions in Section 4.3 and show that our simulated radio sources can be distinguished using the RM. We explore our RM results further and discuss our findings in the context of current and upcoming observing capabilities. In Section 5, we discuss the improvements and limitations of our approach and the implications of our results for AGN jet feedback. We conclude with a summary of our findings in Section 6.

2 SIMULATIONS

The simulations in this study are run with the PLUTO astrophysical fluid dynamics code (version 4.3; Mignone et al. 2007, 2012), using the relativistic magnetohydrodynamics (RMHD) physics module. The simulation set-up used is similar to previous works (Yates-Jones, Shabala & Krause 2021; Yates-Jones et al. 2023), extended to include magnetic fields for both the jet and environment, as described in Section 3. The method used to generate the environment magnetic field follows the approaches described in Huarte-Espinosa et al. (2011a) and Hardcastle & Krause (2014). We used the HLLD Riemann solver, second-order dimensionally unsplit Runge–Kutta time stepping, and linear reconstruction. The $\nabla \cdot \boldsymbol{B} = 0$ condition is controlled by Powell's eight-wave formulation (Powell 1997; Powell et al. 1999), which is used to minimize numerical artefacts on the simulation grid.

These simulations use the publicly available module for PLUTO to include passive Lagrangian tracer particles that are advected with the fluid (Vaidya et al. 2018). To sample the majority of the jet volume, these particles are injected with the jet fluid every 0.01 Myr. They record position, fluid variables, and time since the particle was last shocked (we refer the reader to Yates-Jones et al. 2022, for the details on shock flagging). These quantities are used to calculate synchrotron emissivities using PRAiSE, a modified version of the *Radio AGN in Semi-analytic Environments* (RAiSE; Turner et al. 2018) model. This model takes into account spatially resolved adiabatic, synchrotron, and inverse-Compton losses of synchrotron-emitting electrons. We refer the reader to Yates-Jones et al. (2022) for the full details of the synchrotron emissivity calculation, which is distinct to the method described in Vaidya et al. (2018).

These simulations were carried out on a 3D Cartesian grid centred at (0,0,0). Each dimension contains 5 grid patches: a uniform grid from $-2 \rightarrow +2$ kpc with a resolution of 0.04 kpc/cell; two stretched grid patches from $\pm 2 \rightarrow \pm 10$ kpc; and two stretched grid patches from $\pm 10 \rightarrow \pm 150$ kpc. The high central resolution ensures that the jet injection is sufficiently resolved. The stretched grid patches contain 100 and 150 cells, respectively, with typical resolutions of 0.14 kpc/cell at 10 kpc and 2.01 kpc/cell at 100 kpc. All the simulation grid boundaries are periodic to match our magnetic field initial condition, since the generated environment magnetic fields are periodic by nature.

The simulations are listed in Table 1. We perform five simulations, exploring powerful Fanaroff–Riley type II (FR-II; Fanaroff & Riley 1974) sources. The names of each simulation (QX-DY-BZ[-S]) correspond to the jet power used as $X \times 10^{38}$ W, central environment density as $Y \times 10^{-26}$ g cm^{-3}, and average environment magnetic field strength as Z μG. The '-S' suffix is used to denote our simulation with a different magnetic field structure. Simulation Q6.5-D4-B1 closely resembles Cygnus A. Simulations Q10.8-D1-B1, Q6.5-D4-B2, and Q10.8-D4-B1 change the jet power, environment density, and average environment magnetic field strength to compare the observational signatures in each case. Simulation Q6.5-D4-B1-S is the same as Q6.5-D4-B1 with a different environment magnetic field

Table 1. Parameters of the simulations. $Q_{\rm jet}$ is the one-sided kinetic jet power of the injected jet. $\rho_{0,\,\rm env}$ is the central density of the environment, $\bar{B}_{\rm env}$ is the average environment magnetic field strength, and $k_{\rm min}$ is the minimum non-zero wavenumber on the simulation grid (Section 3.2).

Name	$Q_{\rm jet}$ (W)	$\rho_{0,\,\rm env}$ (g cm^{-3})	$\bar{B}_{\rm env}$ (μG)	$k_{\rm min}$ (kpc^{-1})
Q6.5-D4-B1	6.5×10^{38}	4×10^{-26}	1	0.0067
Q10.8-D1-B1	10.8×10^{38}	1×10^{-26}	1	0.0067
Q6.5-D4-B2	6.5×10^{38}	4×10^{-26}	2	0.0067
Q10.8-D4-B1	10.8×10^{38}	4×10^{-26}	1	0.0067
Q6.5-D4-B1-S	6.5×10^{38}	4×10^{-26}	1	0.02

structure (see Section 3.2). We have chosen these parameters to explore the jet and environment parameter degeneracy for sources similar to the archetypal Cygnus A.

We use an average cluster magnetic field strength of 1 μG in simulations Q6.5-D4-B1, Q10.8-D1-B1, Q10.8-D4-B1, and Q6.5-D4-B1-S; and we use 2 μG for simulation Q6.5-D4-B2. The Cygnus A cluster magnetic field strength is estimated to be ~ 5 μG (Carilli & Barthel 1996) on average. The lower magnetic field strengths are more representative of a typical FR-II radio galaxy environment (Carilli & Taylor 2002). This lower magnetic field also assists with numerical stability in the less dense environment of simulation Q10.8-D1-B1. In this lower density environment, a 5 μG magnetic field would be dynamically important. Combined with the diffusion of the magnetic field, such a strong field would alter the density and pressure of the environment and introduce transonic flows on the simulation grid.

Our simulations were run using the *kunanyi* high performance computing facility provided by Digital Research Services, IT Services at the University of Tasmania. Each simulation ran on 1680 Intel cores and took an average CPU time of 320 000 h.

2.1 Environment

The jets are simulated in an idealized environment based on *Chandra* data of the Cygnus A cluster. Snios et al. (2018) use 2.0 Msec of X-ray observations to derive pressure, density, and temperature profiles as shown in their fig. 4. The density and pressure profiles are fitted to an isothermal King profile of the form

$$\rho = \rho_0 \left(1 + \left(\frac{r}{r_c}\right)^2\right)^{-3\beta/2}, \tag{3}$$

shown in Fig. 1. The fitted Cygnus A profile has core radius $r_c = 50$ kpc, $\beta = 0.885$, central density $\rho_0 = 4 \times 10^{-23}$ kg m^{-3}, and central temperature $T_0 = 1.4 \times 10^8$ K. To create a lower density environment for simulation Q10.8-D1-B1, the shape of the cluster profile is kept but ρ_0 is reduced by a factor of 4. Temperature is held constant in all simulations. Simulations Q6.5-D4-B2, Q10.8-D4-B1, and Q6.5-D4-B1-S all use the same cluster density and pressure as simulation Q6.5-D4-B1.

2.2 Jet parameters

The primary jet parameters in our simulations are the kinetic power, speed, and half-opening angle. The jet is injected with a Lorentz factor of 5, corresponding to a speed of $0.98c$. This is consistent with evidence that FR-II sources, including Cygnus A, have initially relativistic jets which drive energy out to kiloparsec scales (Carilli & Barthel 1996; Hardcastle & Croston 2020). VLBI measurements estimate the full jet opening angle for Cygnus A to be $\sim 10^\circ$ on parsec scales (Boccardi et al. 2014, 2016), however, to properly resolve jet injection on kiloparsec scales, we use a half-opening angle of 15°. The jet power in simulations Q6.5-D4-B1, Q6.5-D4-B2, and Q6.5-D4-B1-S is 6.5×10^{38} W, as estimated from X-ray observations of the bow shock surrounding Cygnus A (Snios et al. 2018; see also Kaiser & Alexander 1999). A higher jet power of 10.8×10^{38} W is used in simulations Q10.8-D1-B1 and Q10.8-D4-B1. In Section 4.2, we show that the combination of the higher jet power and lower central density in simulation Q10.8-D1-B1 produces a size-luminosity track similar to simulation Q6.5-D4-B1. We use a fluid tracer to quantify jet-environment mixing. Jet material is injected with a tracer value of 1, while the environment has an initial value of 0.

3 MAGNETIC FIELD SET-UP

3.1 Jet magnetic field

We extend the hydrodynamical set-up of Yates-Jones et al. (2021) as follows. The helical magnetic field in the jet is approximated as toroidal field loops perpendicular to the jet axis within the jet injection region on the simulation grid. This approximation is valid since the toroidal field dominates the poloidal field in the jet collimation region (Pudritz, Hardcastle & Gabuzda 2012). Our toroidal field loops are parametrized in the following way:

$$\begin{bmatrix} B_x \\ B_y \\ B_z \end{bmatrix} = \begin{bmatrix} -\frac{B_0 sin(\phi)\left(x^2+y^2\right)^{\frac{1}{2}}}{r} \\ \frac{B_0 \cos(\phi)\left(x^2+y^2\right)^{\frac{1}{2}}}{r} \\ 0 \end{bmatrix}, \tag{4}$$

where B_0 is the amplitude of the magnetic field at the base of the jet, ϕ is the spherical azimuth angle, x and y are the distances in their respective axes from the jet (z) axis, and r is the distance from the origin along the outside of the jet cone. This set-up ensures numerical stability in the injection region; only the magnetic field at the outer boundary of the injection region defines the simulated jets. These components of the magnetic field are directly assigned to the PLUTO magnetic field variables when the jet is injected into the simulation.

The initial value of the jet magnetic field B_0 is chosen to be 0.15 μG, following Hardcastle & Krause (2014). This corresponds to very low ratios of magnetic energy to kinetic energy in the two types of jets; for the low-powered jets the ratio is $\sim 5 \times 10^{-8}$, whereas for the high-powered jets the ratio is $\sim 3 \times 10^{-8}$. In comparison to other RMHD simulations of AGN jets, Meenakshi et al. (2023) and Mukherjee et al. (2020) simulate jets with this ratio ranging between 0.01 and 0.2, corresponding to the regime where the magnetic field is dynamically important. In contrast, English, Hardcastle & Krause (2016) use ratios $1-4 \times 10^{-4}$, corresponding to a magnetic field that is not dynamically important for source evolution. Similarly, we have chosen our jet magnetic field to be in the dynamically unimportant regime, and we note that there is little change in the jet dynamics with the choice of jet magnetic field strength whilst in this regime. As we are not considering the effect of internal Faraday rotation in these simulations, the details of the jet magnetic field is not crucial to the analyses in this paper.

3.2 Environment magnetic field

We follow the methods of Murgia et al. (2004) and Hardcastle (2013) to generate turbulent magnetic fields in the cluster gas, using a Kolmogorov power spectrum with slope $\zeta = 17/3$. The magnetic field is set up by first generating the magnetic vector potential components in Fourier space. The magnitudes of these vector components are

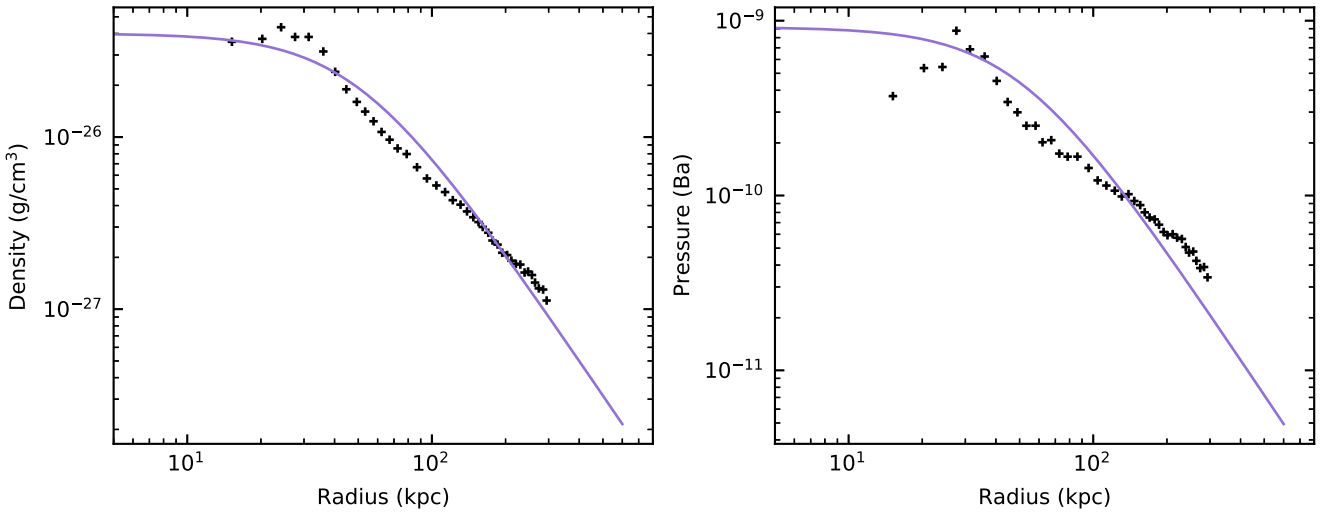

Figure 1. Density (left) and pressure (right) profiles of the Cygnus A cluster. Black crosses indicate data points from fig. 4 of Snios et al. (2018). The data is fitted with an isothermal King profile with temperature 1.4×10^8 K to match the density and pressure on scales of 50–150 kpc.

randomly selected from a Rayleigh distribution with variance $|\mathrm{A}_k|^2$, which is given by

$$|A_k|^2 = \left(k_x^2 + k_y^2 + k_z^2\right)^{-\zeta}. \tag{5}$$

Here, k_x, k_y, and k_z are the wavenumbers in the x, y, and z coordinates. The wavenumber array in each coordinate ($i = x, y, z$) is structured as follows:

$$k_i = [0, k'_{\mathrm{min}}, k'_{\mathrm{min}} - dk, ..., k'_{\mathrm{max}} - dk, \\ -k'_{\mathrm{max}}, -k'_{\mathrm{max}} + dk, ..., -k'_{\mathrm{min}}] \times \frac{2}{x_{\mathrm{max}} - x_{\mathrm{min}}}, \tag{6}$$

where k'_{min} is the unscaled minimum non-zero wavenumber, dk is the linear spacing between wavenumbers, $k'_{\mathrm{max}} = 300$ is the unscaled maximum wavenumber (limited by Nyquist sampling in our 600 x 600 x 600 simulation cube), and the final term is a scaling factor to convert our wavenumbers to kpc^{-1}. In all simulations but Q6.5-D4-B1-S, the minimum non-zero wavenumber k_{min} is set to 0.0067 kpc^{-1} (corresponding to $k'_{\mathrm{min}} = 1$). In simulation Q6.5-D4-B1-S, this is set to 0.02 kpc^{-1} (corresponding to $k'_{\mathrm{min}} = 3$) to generate smaller magnetic field cloud sizes on the grid. Each wavenumber array has the same length as the number of cells in each dimension on the simulation grid.

Next, three amplitude arrays A_i are generated, one for each component of the magnetic vector potential ($i = x, y, z$), which have the same dimensions as the simulation grid. Then, the phase arrays of each magnetic vector component, ϕ_i, have phases randomly drawn from a uniform distribution between 0 and 2π. These phase arrays are then combined with the amplitude arrays to generate the magnetic vector potential, as $\boldsymbol{A}_i = A_i e^{j\phi_i}$ for $i = x, y, i = x, y, z$. The Fourier transform of the magnetic field is then given by

$$\boldsymbol{B}_i = j\boldsymbol{k} \times \boldsymbol{A}_i, \tag{7}$$

where $\boldsymbol{k}$ is the wavenumber vector in three dimensions, $\boldsymbol{A}_i$ are the magnetic vector potential components in Fourier space, and $\boldsymbol{B}_i$ are the magnetic field components in Fourier space. An inverse Fourier transform is performed to find the real values of the magnetic field strength vector components B_x, B_y, and B_z at each point on the given simulation grid. These dimensionless magnetic field vectors are then scaled to realistic galaxy cluster values. A scaling array C and scaling constant D are calculated in CGS units as follows:

$$C = (8\pi p)^{1/2} \;\; ; \;\; D = \frac{\bar{B}_{\mathrm{env}}}{\langle C(B_x^2 + B_y^2 + B_z^2)^{1/2} \rangle}, \tag{8}$$

where $\bar{B}_{\mathrm{env}}$ is the average environment magnetic field strength as shown in Table 1 and p is the environment pressure. The dimensionless magnetic field vectors are multiplied by both C and D to generate the final cluster magnetic field. This is slightly different to the method described in Huarte-Espinosa et al. (2011b), where the authors scale the magnetic vector potential $\boldsymbol{A}_i$ to the radial density profile before taking the curl as in equation (7). Our method may introduce some small errors in $\nabla \cdot \boldsymbol{B}$, which is removed by PLUTO's divergence correction algorithm.

The ratio of the average magnetic field energy density to the average pressure of the environment is calculated to ensure that the magnetic field is less than 10 per cent of the thermal pressure, consistent with expectations for cluster magnetic fields that are not dynamically dominant (Carilli & Taylor 2002). This results in an average environment magnetic field strength on the order of a few μG, which is typical for clusters (Carilli & Taylor 2002). This condition is applied when generating the environment magnetic field which is to be loaded into the simulation as an initial condition. The generated initial magnetic fields for $k_{\mathrm{min}} = 0.0067$ kpc^{-1} and $k_{\mathrm{min}} = 0.02$ kpc^{-1} are shown in Fig. 2. We note that large-scale magnetic fields (in the case of the simulations with $k_{\mathrm{min}} = 0.0067$ kpc^{-1}) are likely to occur in practice, due to the possibility of large-scale coherence caused by cluster weather and gas sloshing from substructure mergers (e.g. Roettiger, Stone & Burns 1999; Takizawa 2008; Vazza et al. 2018; Hu et al. 2023).

4 RESULTS

4.1 Dynamics and implications for the RM results

To show the morphological differences between the simulations, we plot $y - z$ mid-plane slices of the density and x-component of the magnetic field in Fig. 3. Simulation Q6.5-D4-B1 is shown at $t = 15.0$ Myr, simulation Q10.8-D1-B1 is shown at $t = 5.9$ Myr, simulation Q6.5-D4-B2 is shown at $t = 15.2$ Myr, simulation Q10.8-D4-B1 is shown at $t = 12.3$ Myr, and simulation Q6.5-D4-B1-S

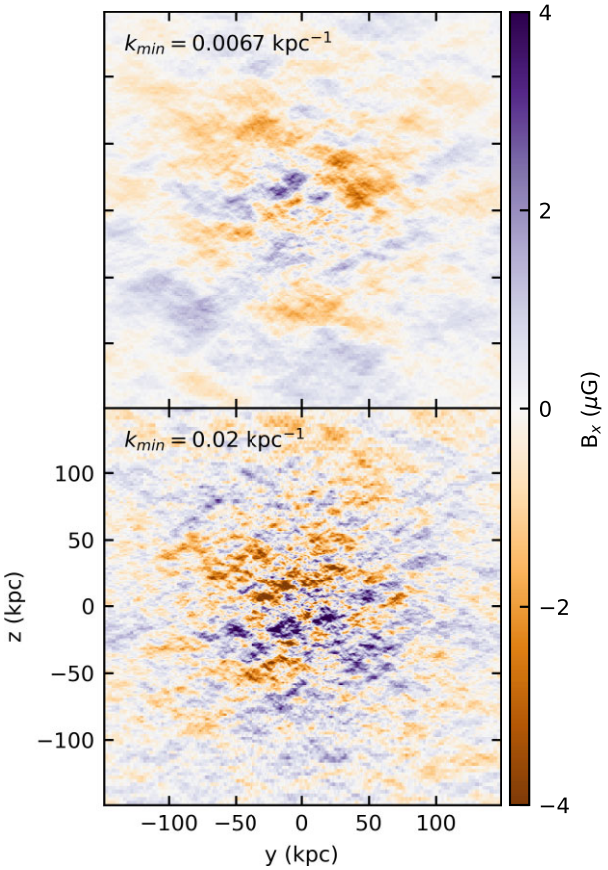

Figure 2. Mid-plane slices at $x = 0$ of the x-component of the initial turbulent magnetic fields. Top: $k_{\rm min} = 0.0067$ ($k'_{\rm min} = 1$). Bottom: $k_{\rm min} = 0.02$ ($k'_{\rm min} = 3$).

is shown at $t = 15.1$ Myr. These times are chosen such that the total extent of their radio emission matches the observed length of Cygnus A in the sky (141.5 kpc; Carilli & Taylor 2002; Turner & Shabala 2019). The details of the length calculation are discussed in Section 4.2.

The morphology of the sources in simulations Q6.5-D4-B1, Q6.5-D4-B2, and Q6.5-D4-B1-S are almost identical, as expected, because the jet power and environment density are the same and the cluster magnetic fields are not dynamically significant (Section 3.2). The morphological differences between these simulations and simulations Q10.8-D1-B1 and Q10.8-D4-B1 correspond to the difference in jet power: the jet power in the latter simulations is 1.7 times higher than that in simulations Q6.5-D4-B1, Q6.5-D4-B2, and Q6.5-D4-B1-S. Due to the higher jet power and lower environment density in simulation Q10.8-D1-B1, the jet propagates faster. This results in narrower lobes as the backflow has had less time to fill them out (see e.g. Yates-Jones et al. 2023). In simulation Q10.8-D4-B1, this higher powered jet propagates only slightly faster than its lower powered counterparts, resulting in a morphology more similar to these lower powered jets. Simulations Q6.5-D4-B1, Q6.5-D4-B2, and Q6.5-D4-B1-S have a much slower expansion in the jet direction, so the sources in these simulations are about 2.5 times older than the source in simulation Q10.8-D1-B1 for the same jet length. Despite the difference in jet expansion speeds, all simulations have similar central ($z = 0$) lobe widths (between 40 and 45 kpc) at the snapshots pictured in Fig. 3.

We find that the average Mach number of the bow shock (using the furthest extent of the bow shock along the jet axis from the origin divided by the source age) is 2.9, 6.8, 2.8, 3.4, and 2.8 for simulations Q6.5-D4-B1, Q10.8-D1-B1, Q6.5-D4-B2, Q10.8-D4-B1, and Q6.5-D4-B1-S, respectively. In contrast, the instantaneous Mach numbers are 2.1, 4.8, 2.1, 2.4, and 2.5, respectively. The lower Mach numbers for simulations Q6.5-D4-B1, Q6.5-D4-B2, Q10.8-D4-B1, and Q6.5-D4-B1-S indicate that the bow shocks of the jets in those simulations are weaker than in simulation Q10.8-D1-B1.

The extent of the bow shock defines the region of the environment affected by the jet. As the jet expands supersonically into the cluster environment, its bow shock sweeps up ambient gas into a 'shocked shell' between the bow shock and the low-density jet cocoon (Alexander 2002). Simulations by Huarte-Espinosa et al. (2011a, b) have shown that the cluster magnetic field is compressed and stretched during jet cocoon expansion, amplifying the strength of the magnetic field. The bow shock initially expands self-similarly (Alexander 2002), but the transverse expansion slows as the jet cocoon approaches pressure equilibrium with the environment (Kaiser et al. 1997; Gaibler, Krause & Camenzind 2009). These shocked shells are dependent on the interaction between the jet and its environment.

The differences between the jets in simulations with lower density and higher density environments are clearly shown by the shape and thickness of the shocked shell. The shocked shells in the lower-density environments are both thicker and rounder. These jets are much older than the jet in simulation Q10.8-D1-B1 for the same length, so the bow shocks have had more time to expand laterally. We see a slight difference in the bow shocks for the lower powered jets compared to simulation Q10.8-D4-B1, where the higher-powered jet has a slightly thinner shocked shell (and younger age) at the same source size. Since the shocked shells in the lower-density environment simulations are significantly thicker than in simulation Q10.8-D1-B1 at the same source size, this will influence the strength of the Faraday rotation signal, as shown below.

The shocked shell is a region of enhanced density and magnetic field strength. Therefore, it will have high RM values (equation 2). Following Huarte-Espinosa et al. (2011b), we identify the shocked shell as the Faraday screen. We define this region numerically by using the pressure gradient from the ambient medium to the shocked shell for the outer boundary, and a jet tracer value of 10^{-4} on the inner boundary. A greater Faraday screen thickness corresponds to a greater path length through this amplified density and magnetic field region (equation 2). The median path length through the Faraday screen looking down the negative x-axis is 29.1 kpc for simulation Q6.5-D4-B1, 12.3 kpc for simulation Q10.8-D1-B1, 29.8 kpc for simulation Q6.5-D4-B2, 24.2 kpc for simulation Q10.8-D4-B1, and 29.4 for simulation Q6.5-D4-B1-S. Similar median path lengths in simulations Q6.5-D4-B1, Q6.5-D4-B2, and Q6.5-D4-B1-S are expected, as the dynamics of these simulations are almost identical. The slightly lower median path length in simulation Q10.8-D4-B1 compared to the lower powered jets corresponds to its higher jet power and slightly faster jet advance speed. Since simulations Q6.5-D4-B1, Q6.5-D4-B2, Q10.8-D4-B1, and Q6.5-D4-B1-S have a higher environment density and Faraday screen thickness than simulation Q10.8-D1-B1, we expect that the RM values from the Faraday screen in these simulations will be higher.

We find that the difference in the density values in the Faraday screen between the high density environment simulations and Q10.8-D1-B1 is less pronounced than the difference in environment densities. The higher average and instantaneous Mach number of the bow shock in simulation Q10.8-D1-B1 leads to greater compression

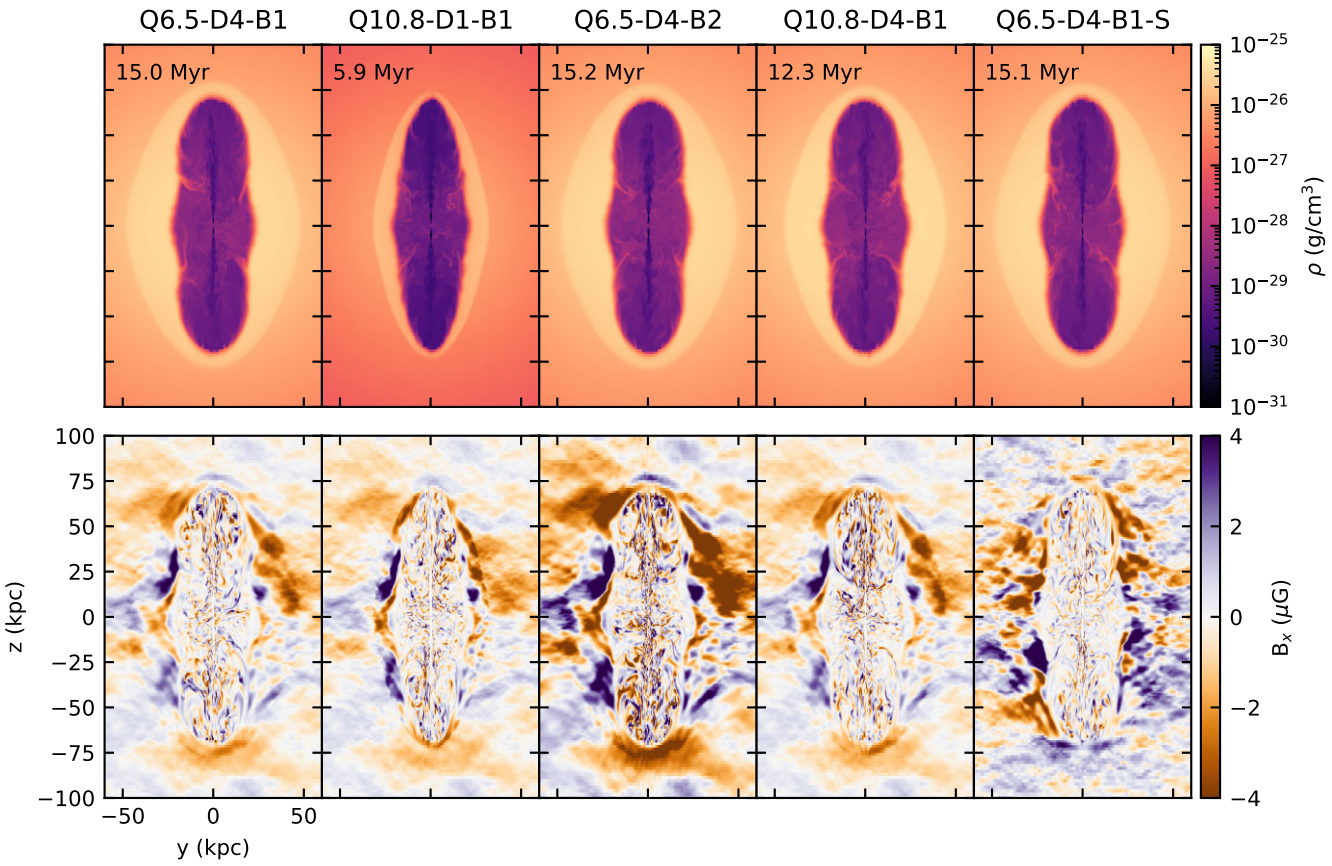

Figure 3. Mid-plane slices at $x = 0$ of density (top) and x-component of the magnetic field (B_x; bottom) for simulations Q6.5-D4-B1, Q10.8-D1-B1, Q6.5-D4-B2, Q10.8-D4-B1, and Q6.5-D4-B1-S (from left to right). Simulation Q6.5-D4-B1 is plotted at 15.0 Myr, simulation Q10.8-D1-B1 is plotted at 5.9 Myr, simulation Q6.5-D4-B2 is plotted at 15.2 Myr, simulation Q10.8-D4-B1 is plotted at 12.3 Myr, and simulation Q6.5-D4-B1-S is plotted at 15.1 Myr.

and a more effective increase in the gas density. This is shown by the higher mean density amplification ratio in this simulation compared to simulations Q6.5-D4-B1, Q6.5-D4-B2, Q10.8-D4-B1, and Q6.5-D4-B1-S (Table 2). However, due to the lower ambient density, the mean density in the Faraday screen of simulation Q10.8-D1-B1 is still less than half that of the mean density in the Faraday screens of the higher density environment simulations (Table 2). There is little difference in the density amplification ratio between the higher and lower powered jets in the high density environment. Additionally, there are no differences in the density and the density amplification due to magnetic field structure size. The Faraday rotation signal from simulation Q10.8-D1-B1 is expected to be lower than that of the sources in higher density environments.

The bow shock driven by the jet also amplifies and sweeps out the magnetic field. Simulation Q6.5-D4-B2 has an ambient magnetic field that is twice as strong as in simulations Q6.5-D4-B1, Q10.8-D1-B1, Q10.8-D4-B1, and Q6.5-D4-B1-S. This difference increases the median x-component magnetic field value in the Faraday screen, which agrees with the findings of Huarte-Espinosa et al. (2011a, b). For simulation Q6.5-D4-B1-S, we find that this median magnetic field strength is slightly higher than but still consistent with simulation Q6.5-D4-B1. We expect the RM values in simulation Q6.5-D4-B2 to be higher than in the simulations with lower magnetic field strength environments, as we confirm in Section 4.3.

4.2 Radio emission at 151 MHz

In the top row of Fig. 4, we show synthetic surface brightness images of the five simulations at 151 MHz. This synthetic emission is generated using the PRAiSE code (Yates-Jones et al. 2022), which is based on the analytical modelling work by Turner et al. (2018) (for a detailed description of the mathematics and computational implementation of this modelling, the reader is directed to these works). We adopt parameters consistent with Cygnus A, placing our simulated sources at a redshift of 0.056075 (Owen et al. 1997) and at a 15° (where the upper jet is tilted away from the reader) viewing angle (Boccardi et al. 2016). We used minimum and maximum Lorentz factors $\gamma_{\rm min} = 600$ and $\gamma_{\rm max} = 1.3 \times 10^5$ (McKean et al. 2016), an equipartition factor $\eta = 0.12$, and an injection index $\alpha_{\rm inj} = 0.7$ (to approximate the 151 MHz–327.5 MHz spectral index; Steenbrugge, Heywood & Blundell 2010). Our beam FWHM is 4.45 arcsec. Here, we define the spectral index as $S_\nu \propto \nu^{-\alpha}$.

We plot each simulation at the time where the total projected lobe length corresponds to the observed extent of Cygnus A, 141.5 kpc. Following Yates-Jones et al. (2023), we calculate these projected lengths from the surface brightness as the distance from the jet injection point to the furthest point of emission, where this furthest point of emission is two orders of magnitude below the maximum surface brightness. The total length is the sum of the jet and counter-jet lengths.

Table 2. Top to bottom: Faraday screen values of; mean density amplification ratio, mean density, median magnitude of the x-component of the magnetic field, volume, mass, and mass percentage. The mass percentage is taken as the Faraday screen mass divided by the total mass within 150 kpc at $t = 0$ Myr. These values are taken at 15.0, 5.9, 15.2, 12.3, and 15.1 Myr for simulations Q6.5-D4-B1, Q10.8-D1-B1, Q6.5-D4-B2, Q10.8-D4-B1, and Q6.5-D4-B1-S, respectively. ρ_e is the density within the region of the Faraday screen taken at the nearest time in an environment-only run of each simulation (e.g. 15, 6, 15, 12, and 15 Myr, respectively).

Simulation name	Q6.5-D4-B1	Q10.8-D1-B1	Q6.5-D4-B2	Q10.8-D4-B1	Q6.5-D4-B1-S
Mean $\frac{\rho}{\rho_e}$	1.2 ± 0.4	1.6 ± 0.7	1.2 ± 0.4	1.3 ± 0.5	1.2 ± 0.4
Mean ρ (10^{-26} g cm^{-3})	2.5 ± 0.9	1.0 ± 0.4	2.5 ± 0.8	2.8 ± 1.0	2.5 ± 0.9
Median $\lvert B_x \rvert$ (μG)	1.0 ± 0.9	1.3 ± 1.2	2.0 ± 1.7	1.0 ± 0.9	1.3 ± 1.2
Volume (kpc^3)	5.7×10^5	1.6×10^5	5.9×10^5	4.5×10^5	5.9×10^5
Mass ($M_\odot$)	2.1×10^{11}	2.5×10^{10}	2.2×10^{11}	1.8×10^{11}	2.2×10^{11}
$\frac{M_{\rm screen}}{M_{150}}$	20.7 per cent	9.80 per cent	21.2 per cent	18.2 per cent	21.2 per cent

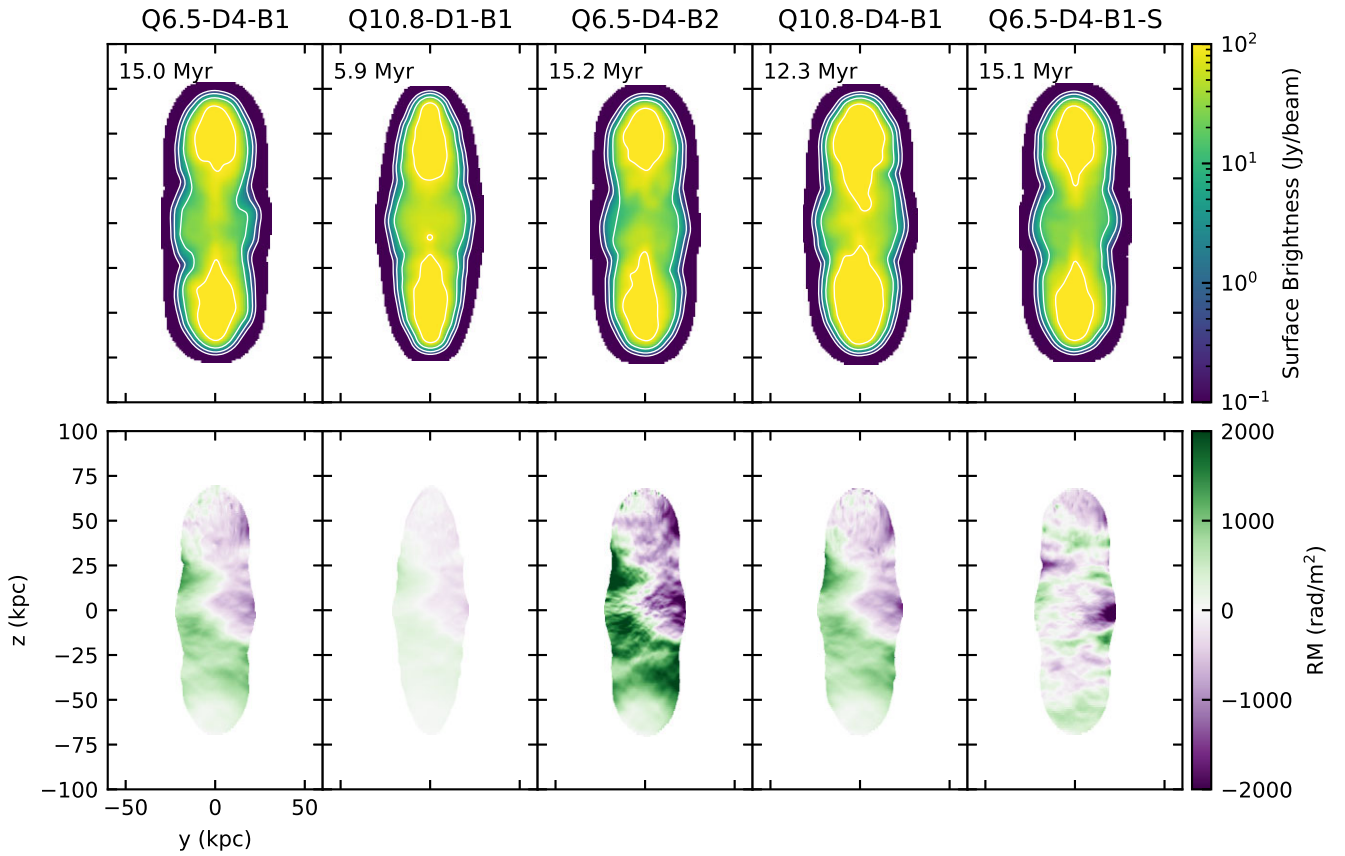

Figure 4. Top: Surface brightness at 151 MHz for simulations Q6.5-D4-B1, Q10.8-D1-B1, Q6.5-D4-B2, Q10.8-D4-B1, and Q6.5-D4-B1-S. Contours are shown for 0.1, 1, 10, 100 Jy beam^{-1}. We take a beam size of 4.45 arcsec. All sources have been tilted by 15°, where the upper jet is tilted away from the reader. Bottom: Rotation measure integrated along the (tilted) positive x-axis. Simulation Q6.5-D4-B1 is plotted at 15.0 Myr, simulation Q10.8-D1-B1 is plotted at 5.9 Myr, simulation Q6.5-D4-B2 is plotted at 15.2 Myr, simulation Q10.8-D4-B1 is plotted at 12.3 Myr, and simulation Q6.5-D4-B1-S is plotted at 15.1 Myr.

At these snapshots, the 151 MHz morphology of each simulation is quite similar. Each simulation exhibits FR-II-like morphology of edge-brightened lobes, as well as hotspot-like features. The lobes of simulations Q6.5-D4-B1, Q6.5-D4-B2, and Q6.5-D4-B1-S are more 'pinched' than simulation Q10.8-D1-B1's lobes, with less emission in the central regions. The underlying properties of these sources would be difficult to distinguish based upon their appearance alone. We note that Q10.8-D4-B1 is visibly brighter in its surface brightness map, due to its increased jet power in comparison to the low-powered sources in the same environment.

We plot the size–luminosity tracks of each source in Fig. 5. The tracks for each simulation except Q10.8-D4-B1 are similar to each other and broadly consistent with the 151 MHz luminosity of Cygnus A at a projected length of 141.5 kpc. The derived ages of each of these similar simulations, 15.0, 5.9, 15.2, and 15.1 Myr are also broadly consistent with Cygnus A age estimates of 6–30 Myr (Carilli et al. 1991; Carilli & Barthel 1996; Kaiser & Alexander 1999). This consistency indicates that the simulation parameters chosen are acceptable for comparison to powerful radio galaxies. The luminosity at a given size for the four similar simulations remains within a range of ±15 per cent of each other after a total projected length of 70 kpc

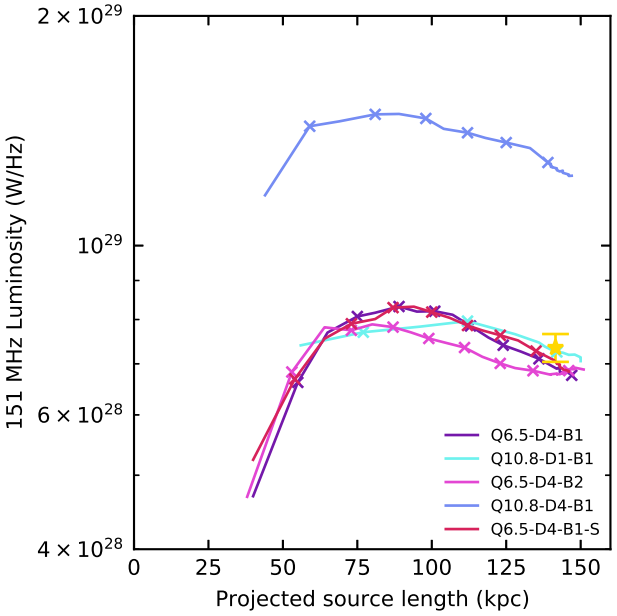

Figure 5. Size–luminosity tracks for simulations Q6.5-D4-B1, Q10.8-D1-B1, Q6.5-D4-B2, Q10.8-D4-B1, and Q6.5-D4-B1-S at 151 MHz. The gold star corresponds to Cygnus A, with a total projected length of 141.5 kpc (Turner & Shabala 2019) and 151 MHz radio luminosity of $7.3 \pm 0.3 \times 10^{28}$ W Hz^{-1} (Baars et al. 1977). Crosses indicate projected lobe lengths every 2 Myr. Simulations Q6.5-D4-B1, Q10.8-D1-B1, Q6.5-D4-B2, Q10.8-D4-B1, and Q6.5-D4-B1-S meet the projected Cygnus A length at 15.0, 5.9, 15.2, 12.3, and 15.1 Myr, respectively.

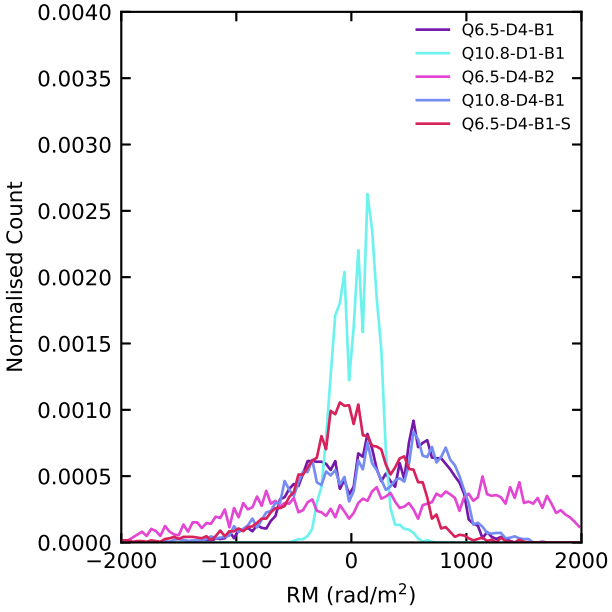

Figure 6. RM distributions for simulations Q6.5-D4-B1, Q10.8-D1-B1, Q6.5-D4-B2, Q10.8-D4-B1, and Q6.5-D4-B1-S. All jets have been tilted to a viewing angle of 15°, where the upper jet is tilted into the page. The RM is integrated down the (tilted) positive x-axis. The jet is oriented along the z-axis.

is reached. Without extra information about the environment, these sources are effectively identical to one another based on their size-luminosity tracks alone. In Section 4.3, we show that these four sources (from simulations Q6.5-D4-B1, Q10.8-D1-B1, Q6.5-D4-B2, and Q6.5-D4-B1-S) can be distinguished using Faraday rotation measure information.

4.3 Faraday rotation

The Faraday rotation measures are calculated directly from the simulation fluid variables. We integrate equation (2) through lines of sight that pass through jet material, calculating two separate RM components: the undisturbed external medium, and the Faraday screen. Here, we take lines of sight down the (tilted) x-axis to calculate spatially resolved maps in the $y - z$ plane of the simulation grid. The external RM component is calculated from the edge of the simulation grid to the edge of the Faraday screen. We distinguish between the jet and ambient media using a fluid tracer threshold of 10^{-4} (e.g. Hardcastle & Krause 2013; Yates, Shabala & Krause 2018). As detailed in Section 4.1, we distinguish between the Faraday screen and the undisturbed environment by calculating the pressure gradient from the ambient medium to the shocked shell.

The bottom row of Fig. 4 displays the RM maps for each simulation at the same snapshots as in Fig. 3. We have interpolated the RM from the raw data on the stretched simulation grid to a uniform observing grid with resolution 1 kpc (corresponding to 0.889 arcsec at z = 0.056075). The interpolation to the observing grid for resolutions of 1 kpc or better does not impact the morphology of the RM map significantly. The jet axis is tilted by 15 deg for each simulation so that the upper jet is tilted away from the reader. Although the initial magnetic field structure is identical across all simulations except Q6.5-D4-B1-S (and hence the broad structure of the RM is also the same), there are significant differences in the *magnitude* of the RM maps. The range of total RM values reached in simulations Q6.5-D4-B1, Q10.8-D1-B1, Q6.5-D4-B2, Q10.8-D4-B1, and Q6.5-D4-B1-S is (−1480, 1650), (−495, 680), (−2732, 2871), (−1611, 1544), and (−3395,1492) rad m^{-2}, respectively. Recent polarization observations of Cygnus A from Sebokolodi et al. (2020) found RMs ranging between −4500 and +6400 rad m^{-2} in the eastern lobe and −5000 to +3000 rad m^{-2} in the western lobe (corresponding to our top and bottom lobes, respectively); the RMs in simulation Q6.5-D4-B2 is most similar to these Cygnus A values.

To demonstrate the differences in RM between the simulations, we plot the distribution of RM values for each simulation in Fig. 6. Each distribution has a centre close to zero, but they have different widths. The mean and standard deviation for simulations Q6.5-D4-B1, Q10.8-D1-B1, Q6.5-D4-B2, Q10.8-D4-B1, and Q6.5-D4-B1-S are 185 ± 525, 49 ± 170, 346 ± 1048, 187 ± 576, and −48 ± 518 rad m^{-2}, respectively. We use the full width at half-maximum (FWHM) of the RM distribution to measure the differences between our simulations. We calculate FWHMs of 1478 ± 47, 470 ± 8, 3240 ± 264, 1610 ± 49, and 1176 ± 21 rad m^{-2} in simulations Q6.5-D4-B1, Q10.8-D1-B1, Q6.5-D4-B2, Q10.8-D4-B1, and Q6.5-D4-B1-S, respectively.

Comparing simulation Q6.5-D4-B1 to simulation Q10.8-D1-B1, we see that increasing the environment density by a factor of 4 broadens the distribution by a factor of approximately 3. Furthermore, the increase in the distribution width from simulation Q6.5-D4-B1 to simulation Q6.5-D4-B2 shows us that increasing the magnetic field strength by a factor of 2 also broadens the distribution by a factor of approximately 2. In both cases, these environmental increases amplify the extreme values of the RM. Therefore, we have shown that we can distinguish between our simulations with similar Stokes I properties (Figs 4 and 5) using the RM values. We note that the RM distributions for Q6.5-D4-B1 and Q10.8-D4-B1 are almost identical,

indicating that the difference in environment density impacts the RM more than the factor of 1.7 in jet power.

The RMs in simulations Q6.5-D4-B1 and Q6.5-D4-B1-S are distinct from one another, as seen most clearly in Fig. 6. For simulation Q6.5-D4-B1-S and its smaller magnetic field structures, we see a narrower distribution. This behaviour is expected, as for decreasing size of the magnetic field structures, the magnetic field that is backlit by the radio source will be increasingly isotropically random. This results in a smaller FWHM for the RM distribution for simulation Q6.5-D4-B1-S. Therefore, the details of the magnetic field structure of the ambient environment do influence the RM properties, in addition to the magnitude of the magnetic field and the environment density.

4.3.1 RM as a probe of environment

The distinction between the Faraday rotation measures allows us to break the degeneracy in the observable radio properties of simulations Q6.5-D4-B1, Q10.8-D1-B1, Q6.5-D4-B2, and Q6.5-D4-B1-S, using the Faraday rotation as a probe of the radio galaxy environment. We can also study the effect of jet power in the higher density environment using our brighter source from simulation Q10.8-D4-B1, and the effect of the magnetic field structure using simulation Q6.4-D4-B1-S.

We plot the components of the RM for our simulations in Fig. 7. The first two columns correspond to the two components (external and Faraday screen) that make up the total RM (third column) for our simulations. The fourth column corresponds to the 'reference' RM at $t = 0$ Myr using the same integration limits as for the total RM; in practice, this is calculated by using the same definitions of the ambient medium and shocked shell as for the age of interest for each simulation, but calculating the RM values at time $t = 0$ Myr. This comparison may also be done with an evolved environment (i.e. an equivalent simulation without a jet) at the same age for each source; however, we found that the differences between the two approaches are negligible for all five simulations. The fifth column ('difference' RM) corresponds to the difference between the total RM and the reference RM. We ignore the internal Faraday rotation component in this case, as we find that the RM in the low-density cocoon is negligible and the amount of entrained thermal plasma is low. We note that the external RM component does not include any chance line-of-sight sources that may be present in real observations.

The dominant component of the total RM in all cases is the Faraday screen. However, in simulation Q10.8-D1-B1, the external RM is more comparable to the Faraday screen RM. In this case, the Faraday screen is approximately a factor of 2 thinner than the screens in simulations Q6.5-D4-B1, Q6.5-D4-B2, Q10.8-D4-B1, and Q6.5-D4-B1-S, and the mean density is lower (Section 4.1). In all five simulations, we see similar features in the Faraday screen RMs, particularly at the lobe edges and in the upper jet (which is tilted away from the reader).

We see that the overall magnitude of the RM is not markedly different when a radio source is present. This is consistent with the findings of Huarte-Espinosa et al. (2011b), who primarily find RM enhancements towards the edges of the visible lobe. As the jet pushes out the magnetic field, it aligns the field with the shape of the cocoon. At the edges, this magnetic field alignment will be closer to the line of sight of the RM calculation (see Fig. 3). These edge enhancements can be seen in the 'difference' RMs in Fig. 7. Edge-enhanced RMs have also been reported in recent observations of the Spiderweb Protocluster (Anderson et al. 2022).

Simulation Q6.5-D4-B1-S shows smaller RM structures to the other simulations, but these structures are of a similar range of magnitudes across the source to the larger structures seen in simulation Q6.5-D4-B1 (Fig. 6). We note here that while the magnetic field has a different structure and different random seed in these two simulations, there is a similar spot of negative RM on the right-hand side of the lobe at $z \sim 0$. The 'difference' RM maps show that this spot is purely due to the environment, not due to the action of the jet.

Our rotation measure maps (Figs 4 and 7) for simulations Q6.5-D4-B1, Q10.8-D1-B1, Q6.5-D4-B2, and Q10.8-D4-B1 show a clear RM sign reversal across the jet (i.e. in the y-direction). The RM in the upper lobe has a clear divide between positive and negative RMs on either side of the jet ($z -$)axis. Reversals not aligned with the jet axis can be seen in the 'reference' RM maps (i.e. without a jet present), which is expected from the presence of the larger scale modes in the assumed power spectrum. However, we also see in the Faraday screen and total RMs that the jet acts to align this reversal with the jet axis, particularly in the upper lobes ($+z$), which are tilted away from the reader. This is due to the action of the jet compressing and amplifying the ambient magnetic field in the Faraday screen, inducing a change in the field distribution. A similar reversal can also be seen in the western lobe of Cygnus A (fig. 9 of Sebokolodi et al. 2020) and the Spiderweb Protocluster (Anderson et al. 2022). We do not see a clear reversal in the same manner for simulation Q6.5-D4-B1-S, indicating that this may be an effect we are only seeing due to the particular magnetic field structure in the other simulations.

The lower lobes ($-z$) are tilted towards the reader and have lower values of RM at the tip. This matches the expectation of the Laing-Garrington effect (Garrington et al. 1988; Laing 1988), which predicts that the radio lobe pointed further away from the observer will have greater RM values and therefore be more subject to depolarization. This lobe will have a greater path length through the magneto-ionized medium (external + screen), which will act to increase the magnitude of the RM. We note that the prominent large-scale field fluctuations in magnetic fields with lower minimum wavenumbers may lead to RM distributions that differ from the Laing–Garrington expectation; the details depend on the magnetic field structure. Anisotropic fields can be found when the observing window is similar to the correlation length of the magnetic field (Enßlin & Vogt 2003). This correlation length is calculated by (Enßlin & Vogt 2003; Loi et al. 2019)

$$\Lambda_B = \frac{3\pi}{2} \frac{\int_0^\infty |B_k|^2 k \mathrm{d}k}{\int_0^\infty |B_k|^2 k^2 \mathrm{d}k}, \tag{9}$$

where k is the wavenumber and $|B_k|^2$ is the Fourier transform of the magnitude of the magnetic field.

The correlation length for Cygnus A is estimated to be 30 kpc (Carilli & Taylor 2002). Magnetic fields with similar correlation lengths to that in the Cygnus cluster are unstable on the stretched grid that we use. Simulation Q6.5-D4-B1-S, with $k_{\rm min} = 0.02$ kpc^{-1}, has a correlation length of approximately 96 kpc; all four other simulations with $k_{\rm min} = 0.0067$ kpc^{-1} have a correlation length ~310 kpc. While the correlation length for simulation Q6.5-D4-B1-S is about a factor of 3 higher than the Cygnus A correlation length, it is roughly a factor of 3 lower than that for the four other simulations. The correlation length for $k_{\rm min} = 0.0067$ kpc^{-1} is larger than the total length of our jets, 141.5 kpc, and so the magnetic field within the jet observing window will not be isotropic. For simulation Q6.5-D4-B1-S, the correlation length is shorter than the jet length, and so the magnetic field within the jet observing window will be closer to being isotropic

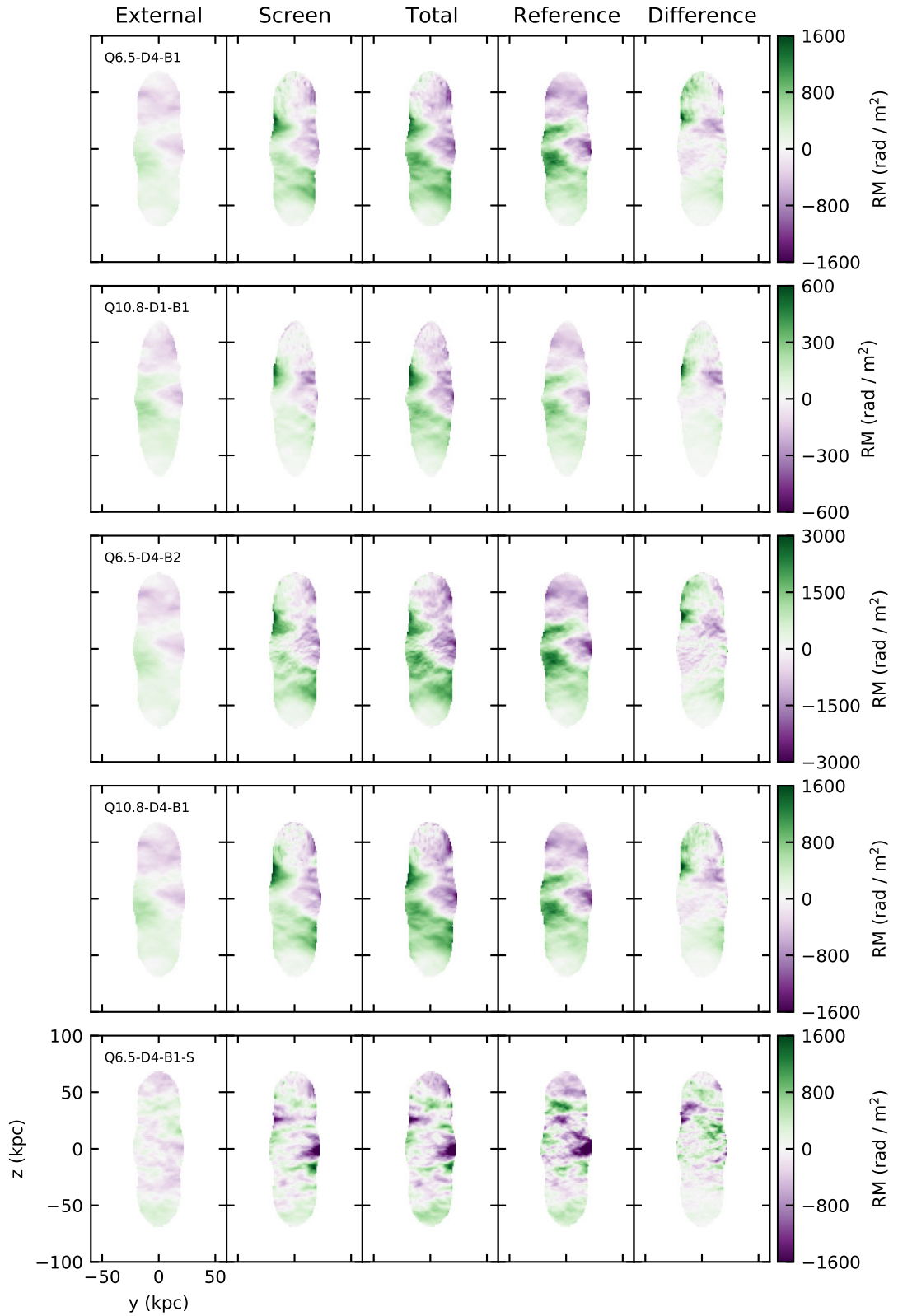

Figure 7. Spatial distributions of the separated components of the rotation measure. From left to right, we plot the external component, the Faraday screen component, and the total sum of these two. In the fourth column, we plot the 'reference' RM at $t = 0$ Myr using the jet tracer from each simulation's time of interest. The final column is the difference between the total RM and the reference RM. As in Fig. 4, RM is integrated along the (tilted) positive x-axis. The jet is oriented along the z-axis and is tilted at a viewing angle of 15° into the page, where the upper jet is tilted away from the reader. From top to bottom, we plot simulation Q6.5-D4-B1 at 15.0 Myr, simulation Q10.8-D1-B1 at 5.9 Myr, simulation Q6.5-D4-B2 at 15.2 Myr, simulation Q10.8-D4-B1 at 12.3 Myr, and simulation Q6.5-D4-B1-S at 15.1 Myr.

than for the other four simulations. We see this reflected in the lack of a clear decrease in RM values at the tip of the lower jet (Fig. 7).

This decrease in RM values for the large correlation length simulations is a chance effect due to the orientation of the observer. The viewing angle reduces the path length through the environment to the lower lobe, which therefore reduces the amount of rotating material along that line of sight. This affects the longer correlation length simulations more, since there are fewer magnetic reversals along the path length. We find that the reduction of the Laing-Garrington effect for the shorter correlation length simulation is independent of the observing direction (i.e. the axis the RM is integrated along).

Since both the external and Faraday screen RMs are dependent on the environment magnetic field, modelling this field accurately is important for making comparisons to RM observations. Not only does the seed magnetic field make a difference to the spatial RM distribution, but the line of sight chosen for the RM integration (e.g. *x*-axis or *y*-axis) can also make a significant difference, especially in the case of an anisotropic field as we have for our simulations with $k_{\rm min} = 0.0067$ kpc^{-1}. This aspect of modelling cluster magnetic fields is an area for improvements to be made in the future.

4.3.2 *Observability of the RM differences*

We now consider which differences in the RM maps of our simulations are observable with a telescope. In Fig. 8, we show the effects of sensitivity and resolution on our RM maps. In the first column, we show the total RM maps from Fig. 4. In the second column, we show this RM map convolved with a 4.45 arcsec beam. The third column shows the visible data using a dynamic range of 10 at 151 MHz;[1] we consider this to be a lower limit on dynamic range to study here. The dynamic range is implemented by applying a threshold to the surface brightness image; we only include pixels in the RM map that are above one-tenth of the brightest pixel of the surface brightness image.

The primary difference between these synthetic observations and the total RM maps is when the dynamic threshold is applied; if the instrument has low sensitivity, information mostly from the oldest electrons, primarily in the equatorial regions of the lobe, is lost. This will affect the most extreme RM values in the distribution, as shown in Fig. 9, where the FWHMs of the RM distributions are largely unaffected by the differences in sensitivity. We estimate that most reasonable dynamic ranges at 151 MHz would be sufficient to capture the FWHM differences; we do not find significant departures from the distribution shape for dynamic ranges $\gtrsim$10.

To be able to observe the RMs, we must also consider what frequencies the RMs will be visible at. This may be characterized using the depolarization frequency, where the fractional polarization drops to half of its high-frequency value, as given by Krause, Alexander & Bolton (2007):

$$\nu_{1/2} = \sqrt{\frac{\sigma_{\rm RM}}{13}}\ {\rm GHz}, \tag{10}$$

where $\sigma_{\rm RM}$ is the RM dispersion, which we take to be the standard deviation of $812 n_e \boldsymbol{B} \cdot dl$ rad m^{-2} along each line of sight. Equation (10) is based on an analysis of multi-scale magnetic fields with high-resolution data cubes as opposed to the classical Burn (1966) law, which assumes a two-scale field.

We show spatial RM dispersion and depolarization frequency maps in Fig. 10. The spatial structure of both $\sigma_{\rm RM}$ and $\nu_{1/2}$ are similar to the total RM structures shown in Fig. 4, with enhanced regions to the sides of the lobes and a decrease towards the jet axis and lobe ends. This indicates that emission from the most recently shocked electrons near the jet hotspots will depolarize at lower frequencies than the electrons in the backflow. In simulation Q6.5-D4-B1-S, this decrease in depolarization frequency is more subtle, indicating that the magnetic field structure can influence this result. The depolarization frequencies are $\lesssim$1.5 GHz for each of our sources; we find the maximum and median depolarization frequency in simulations Q6.5-D4-B1, Q10.8-D1-B1, Q6.5-D4-B2, Q10.8-D4-B1, and Q6.5-D4-B1-S to be 1116, 640, 1579, 1169, 1441 MHz and 649, 345, 965, 679, 713 MHz, respectively. Therefore, the RMs could only be entirely observed by instruments operating above $\gtrsim$1.5 GHz. However, since there are a range of different depolarization frequencies across the source, the source will progressively depolarize, and the RM can still be characterized at MHz frequencies.

We quantify the observability of the FWHM of the RM distribution at MHz frequencies in Fig. 11. We plot the measured FWHMs of the RM distributions where $\nu_{\rm obs} > \nu_{1/2}$ for the total RM and 'observable' RM maps shown in Fig. 8. We also include an 'observable' RM map convolved with a 8.89 arcsec beam. To estimate the error in our FWHM measurement, we calculate the FWHM with four tolerance levels corresponding to 0.04, 0.06, 0.08, and 0.1 times the distribution peak, taking the mean and standard deviation of these measurements. For all our simulations, we do not find any observable polarized emission at frequencies $\lesssim$ 200 MHz. FWHM values converge for all sources as frequency increases, and the source RM becomes fully visible. Each of our sources begin to lose RM information at lower frequencies, so the measured FWHM falls away from the true value. The frequencies at which the measured FWHM (for the unconvolved total RM) are more than one standard deviation away from the true value for our simulations are $\sim$800, 500, 1000, 900, and 500 MHz for simulations Q6.5-D4-B1, Q10.8-D1-B1, Q6.5-D4-B2, Q10.8-D4-B1, and Q6.5-D4-B1-S, respectively. We note that powerful FR-IIs in poor environments are likely to be more reliably observed at lower frequencies, and stronger cluster magnetic fields result in stronger depolarization at higher frequencies. We also note that the increased jet power in simulation Q10.8-D4-B1 does not alter the depolarization signature significantly, so for our simulations we find that the environment is the main indicator for this depolarization signature. These different depolarization signatures can provide key information about the environment the source resides in.

In the top panel of Fig. 11, we compare the measured FWHM for simulations Q6.5-D4-B1 and Q6.5-D4-B1-S. We find that for the smaller magnetic field clouds, the depolarization effect on the measured FWHM of the RM distribution occurs at lower frequencies. This confirms the result of Meenakshi et al. (2023), who find that larger magnetic field correlation lengths result in increased depolarization by the Faraday screen; we note that the depolarization in their study comes directly from the polarized emission, rather than from the RM dispersion as we have done here. However, the measured FWHMs for both beam sizes behave similarly to the larger magnetic field clouds, with the depolarization beginning to affect the measured FWHM at 800 MHz (within errors for Q6.5-D4-B1-S). The effect of the magnetic field cloud size on the depolarization is more subtle than the effect of environment density and magnetic field strength.

[1]Note that this dynamic range is for one source and does not account for other bright sources in a large field of view. This dynamic range should be consistent with lower surface brightness sources in a field with brighter sources.

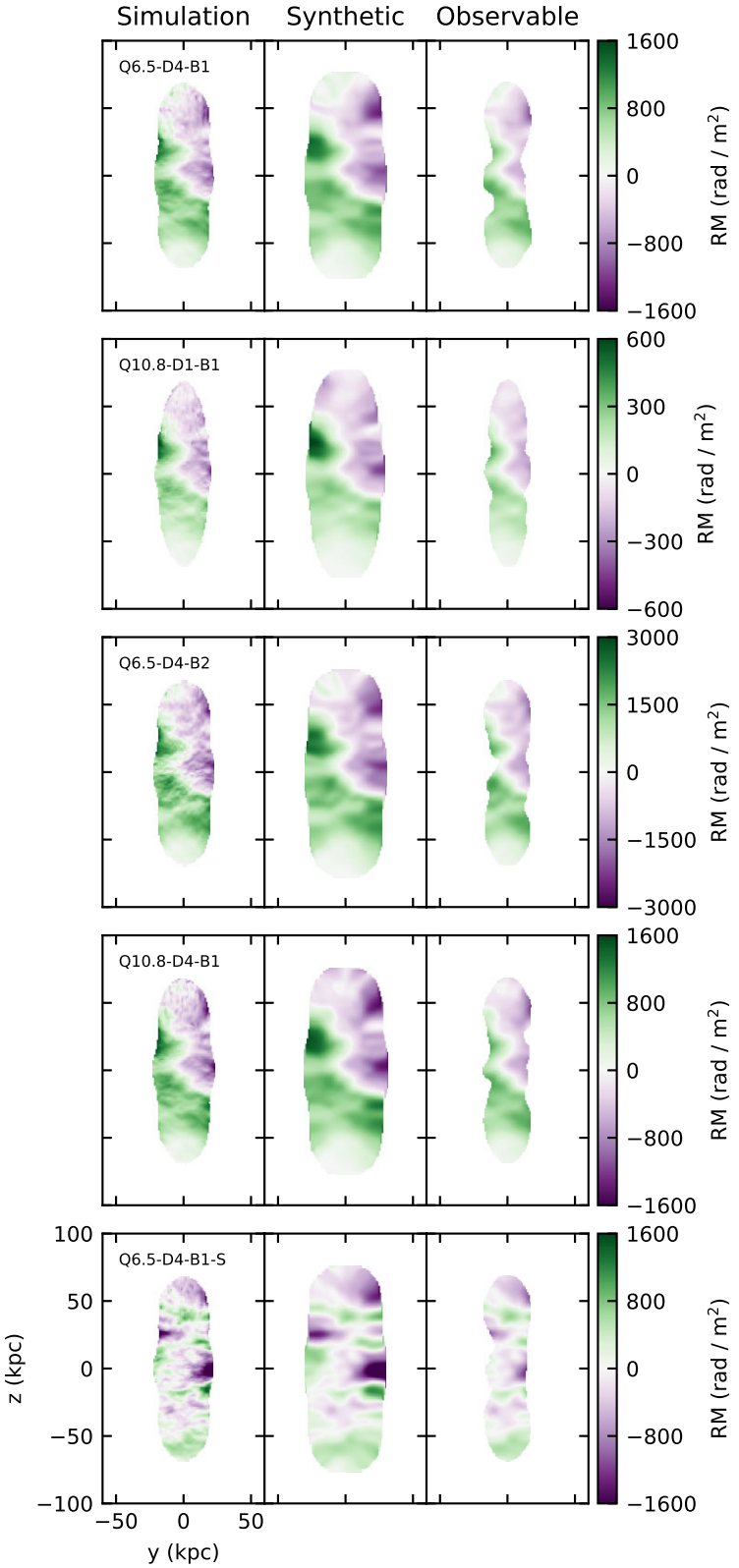

Figure 8. Comparison of RM maps for each synthetic observation as described in the text. From left to right: Total RM, total RM convolved with a 4.45 arcsec beam, and this convolved data with a dynamic range of 10 at 151 MHz applied. From top to bottom, we plot simulation Q6.5-D4-B1 at 15.0 Myr, simulation Q10.8-D1-B1 at 5.9 Myr, simulation Q6.5-D4-B2 at 15.2 Myr, simulation Q10.8-D4-B1 at 12.3 Myr, and simulation Q6.5-D4-B1-S at 15.1 Myr.

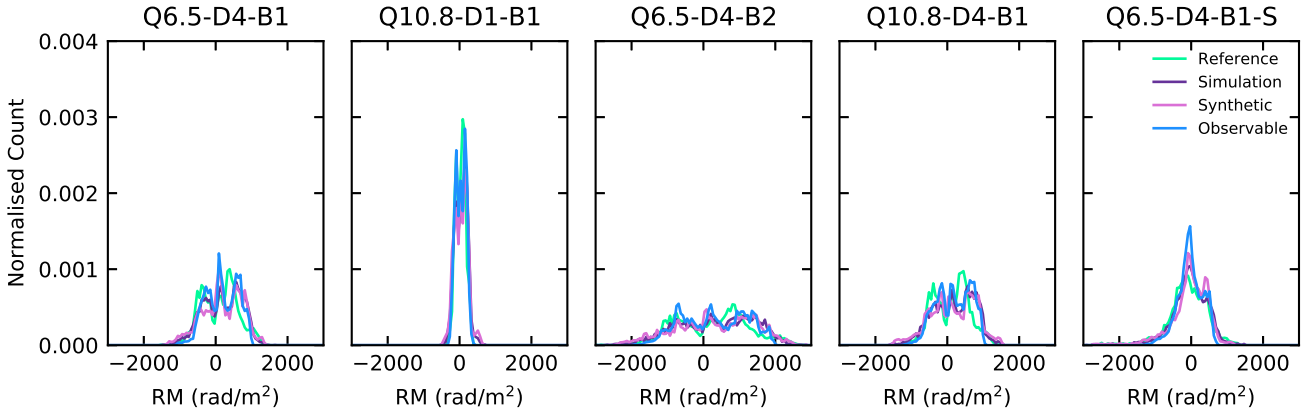

Figure 9. Histograms for the different synthetic observations as shown in Fig. 8, as well as the unaffected environment RM shown in Fig. 7. The 'reference' RM is interpolated to the same observing grid as the 'simulation' RM (resolution 1 kpc/0.889 arcsec) to plot its structure function (Fig. 12). The 'synthetic' RM is the 'simulation' RM convolved with a 4.45 arcsec beam and the 'observable' RM corresponds to this convolved data with a dynamic range of 10 at 151 MHz applied, as seen in Fig. 8.

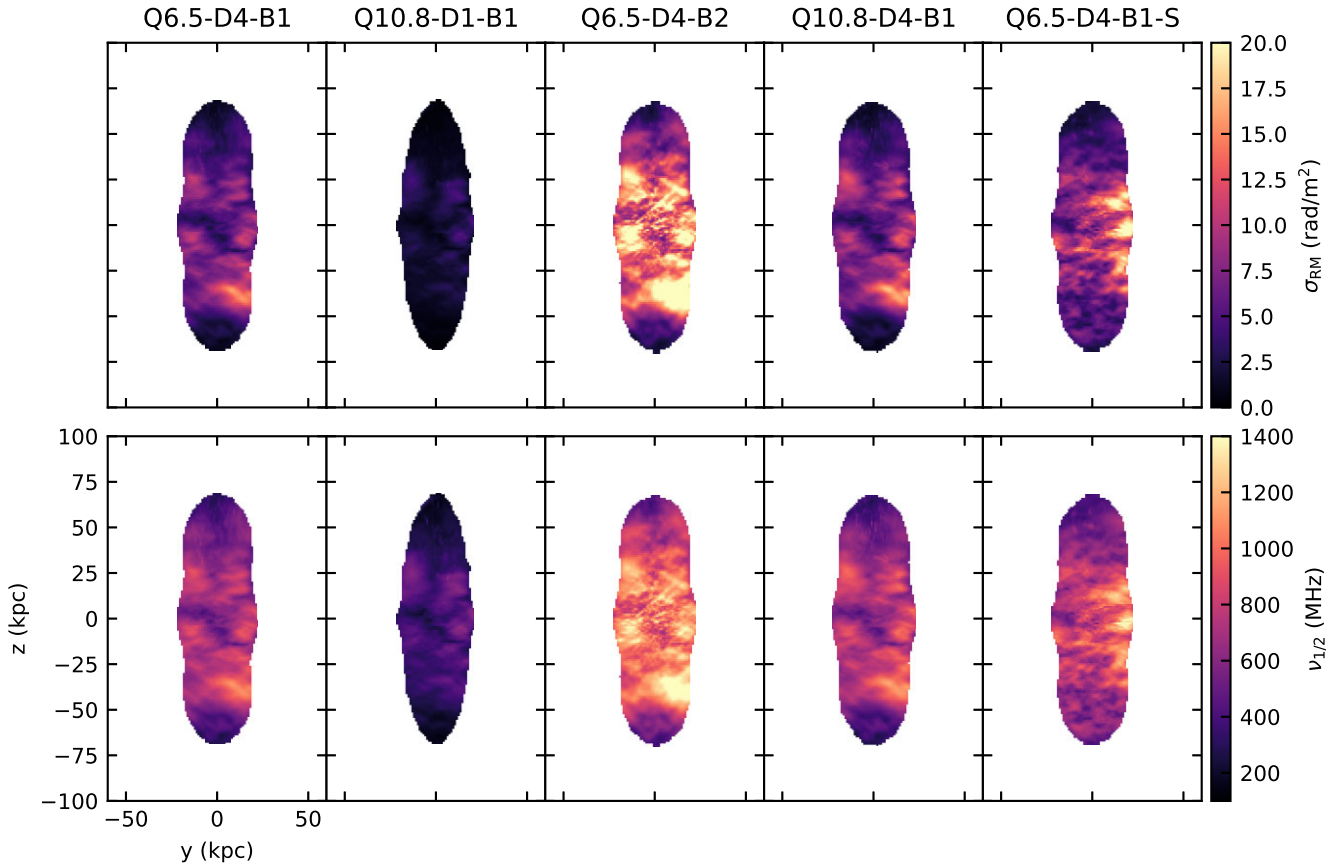

Figure 10. RM dispersions (top) and depolarization frequencies (bottom). Simulation Q6.5-D4-B1 is plotted at 15.0 Myr, simulation Q10.8-D1-B1 is plotted at 5.9 Myr, simulation Q6.5-D4-B2 is plotted at 15.2 Myr, simulation Q10.8-D4-B1 is plotted at 12.3 Myr, and simulation Q6.5-D4-B1-S is plotted at 15.1 Myr.

For these sources observed at 151 MHz, the lower powered jets will not be polarized. The higher powered jet is partially polarized at this frequency, but the measured FWHM is well below the true value. To distinguish between these sources at 151 MHz, we would require polarimetry at higher frequencies. For frequencies $\gtrsim$1 GHz, synchrotron losses will distinguish these particular sources in their surface brightness, but in general, the size–luminosity degeneracy may occur at higher frequencies for different jet powers and environments. The pattern of the measured FWHM of the RM distribution with observing frequency still encodes much information about the environments, even without reconstructing the full RM distribution.

Detecting the differences between different jet power and environment density combinations, as we have shown in this paper, requires sufficient resolution to detect the RM distribution. The 4.45 arcsec resolution used in this paper is optimistic for large surveys of AGN jets (Table 3). We see in Fig. 11 that a reduction in observing

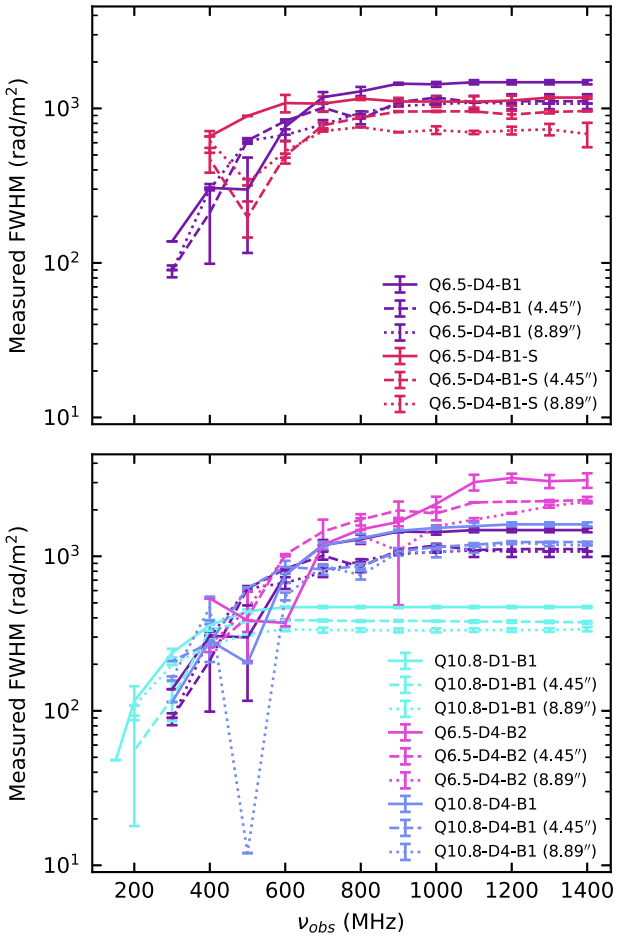

Figure 11. Measured RM FWHM versus observing frequency for simulations Q6.5-D4-B1 and Q6.5-D4-B1-S (top panel), and simulations Q6.5-D4-B1, Q10.8-D1-B1, Q6.5-D4-B2, Q10.8-D4-B1 (bottom panel). Solid lines correspond to the total RM data with the depolarization frequency threshold $\nu_{obs} > \nu_{1/2}$ applied. Dashed 4.45 arcsec lines correspond to the 'observable' RM maps that have been convolved with a 4.45 arcsec beam, with a dynamic range threshold of 10 and the depolarization frequency threshold applied. Dotted 8.89″ lines correspond to the same 'observable' RM maps but convolved with a 8.89 arcsec beam instead.

resolution results in a smaller measured FWHM. However, there are clear differences between the environments considered in our simulations that may still be detected at a lower resolution, if the RM resolution is sufficient. Table 3 lists the key parameters for various polarization surveys, including the RM resolution (i.e. the RMSF FWHM), which ranges from 1.2 rad m^{-2} for LoTSS to 370 rad m^{-2} for Apertif, and the maximum RM scale, which ranges from 0.97 rad m^{-2} for LoTSS to 2500 rad m^{-2} for QUOCKA. For all listed surveys other than LoTSS and POGS, the RM dispersions shown in Fig. 10 are lower than this maximum scale. Hence, for most current surveys, the RM resolution and maximum scale are sufficient to detect the differences between our simulated sources.

With these current surveys, the detection of RMs is primarily limited by survey resolution. However, for poorly resolved sources, Anderson, Gaensler & Feain (2016) show that broad-band depolarization modelling can discern information about the RM distribution at scales beneath the observing beam. This would allow for the detection of the FWHMs and the differences between them in current surveys, particularly for sources at high redshift. Upcoming sky surveys using next-generation instruments such as SKA-low and the ngVLA will have sufficient resolution to study large populations of AGN jets in detail and characterize their environments using polarimetry. In particular, the SKA-low survey will have an RM resolution of ∼0.1 rad m^{-2} (Stepanov et al. 2008) and so will present an opportunity to study even smaller differences in RM than our current surveys.

4.3.3 *Structure functions*

If the spatial RM distribution of an observed source can be measured, we can determine its structure function. The structure function describes the two-dimensional fluctuations of the RM and is given by (Simonetti, Cordes & Spangler 1984; Minter & Spangler 1996; Laing et al. 2008; Guidetti et al. 2012)

$$S(r) = \langle [\mathrm{RM}(r + r') - \mathrm{RM}(r')]^2 \rangle, \tag{11}$$

where r and r' are vectors in the plane of the sky and $\langle\rangle$ is an average over r'. In Fig. 12, we show the structure functions for the 'simulation', 'synthetic', 'observable', and 'reference' RMs shown in Figs 7 and 8. The 'simulation' RM corresponds to the total RM maps shown in Fig. 4. Likewise to the 'simulation' RM, the 'reference' RM has been interpolated to the same uniform observing grid. We compare our structure functions to the Kolmogorov spectrum structure function as given by (Laing et al. 2008)

$$S(r) = \frac{4\pi^{q-1}}{q-2} \frac{\Gamma(2 - q/2)}{\Gamma(q/2)} r^{q-2}, \tag{12}$$

where Γ is the Gamma function, and $2.5 < q < 4$ with $q = 11/3$ for a Kolmogorov spectrum.

The structure functions all roughly follow a power-law increasing slope until the lobe-width scale (second vertical grey line from the left), after which the structure function begins to turn over. The 'observable' RM has some differences compared to the 'simulation' and 'synthetic' RMs. The power in the 'observable' structure function tends to decrease at scales just below the lobe width, with the full signal in the 'simulation' and 'synthetic' RMs remaining a power law until the lobe width is reached. This initial power law does not follow the Kolmogorov spectrum (dark grey dashed lines) in most cases; this is likely due to the simulation resolution and interpolation of the RM.

The structure functions all rapidly decrease towards the lobe-length scale (third vertical grey line from the left), as the number of (r, r') pairs to average over decreases. This flattening from power-law structure has been observed in observations and simulations (Laing et al. 2008; Guidetti et al. 2011b, 2012), however, unlike Huarte-Espinosa et al. (2011b) we find that this change in gradient is not the result of the jet interacting with its environment during source expansion. For all simulations but Q10.8-D1-B1, we show in Fig. 12 that the 'simulation' and 'synthetic' RMs do not depart significantly from the 'reference' RM structure function. We find that it is the shape of the jet cocoon, i.e. the 'RM window', that influences the RM structure function. We note that the environment influences the behaviour of the structure function after the turnover. As the density decreases outside of the core region, so too does the magnitude of the RM. The 'dip' just after the initial turnover occurs at approximately 50 kpc for the 'reference' and 'simulation' structure functions in our large magnetic field structure simulations. Additionally, for different seed magnetic fields, the behaviour of the structure function past the lobe width will change due to the anisotropy across the 'RM window' (as discussed in Section 4.3.1).

We see for simulation Q6.5-D4-B1-S that the structure function behaves more like a broken power law, as it plateaus before the

Table 3. Key parameters for various polarization surveys in progress.

Survey	Frequency (MHz)	Coverage	1-σ rms (μJy beam^{-1})	Resolution (arcsec)	RMSF FWHM (rad m^2)	Max. RM (rad m^2)	Max. scale (rad m^2)	Reference
POSSUM	800−1088	2pi sr	18	13	54	4000	40	1
POSSUM band 2	1130−1430	1.5pi sr	30	11	370	4000	72	1
Apertif	1130−1430	Irregular	16	15	370	4000	72	2
LoTSS	120−168	$-1 < \delta < +90$	70	6	1.2	450	0.97	3
POGS	216	$-82 < \delta < +30$	Varies; 1×10^3–3×10^4	180	6.2	1000	1.9	4
QUOCKA	1300−8500	Targeted pointings	50	Flexible; 1–15	67	90,000	2500	5
VLASS	2000−4000	$-40 < \delta < +90$	69	5	200	2300	560	6

Note. References: (1) Vanderwoude et al. (2024), (2) Adebahr et al. (2022), (3) Shimwell et al. (2022), (4) Riseley et al. (2020), (5) Heald et al. (in preparation), (6) Lacy et al. (2020).

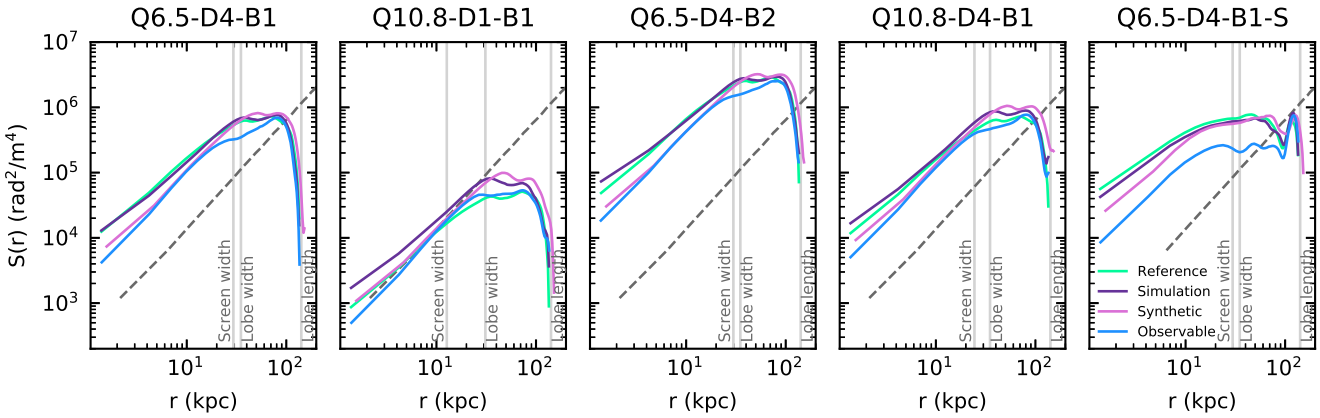

Figure 12. Structure functions for the different synthetic observations as shown in Fig. 8, as well as the unaffected environment RM shown in Fig. 7. The 'reference' RM is interpolated to the same observing grid as the 'simulation' RM (resolution 1 kpc/0.889 arcsec) to plot its structure function. The 'synthetic' RM is the 'simulation' RM convolved with a 4.45 arcsec beam and the 'observable' RM corresponds to this convolved data with a dynamic range of 10 at 151 MHz applied, as seen in Fig. 8. The 'lobe length' is the total projected length of the radio source, 141.5 kpc. The 'lobe width' is the median projected width of the radio lobes. The 'screen width' is the median projected path length through the Faraday screen.

turnover. The turnover still occurs at scales approximately equal to the projected lobe width, but the behaviour after this point is also different. The 'dip' at approximately 50 kpc is the start of a deeper minimum that occurs at approximately 90 kpc, before peaking again prior to the lobe length scale. This different behaviour is due to the different magnetic field structures, both in size and in random seeding.

The structure function only changes significantly for the 'observable' case, where the RM map is dynamic-range limited and loses the full jet cocoon shape (see Fig. 8). We also note that the 'synthetic' RM structure function has its initial turnover at a slightly larger scale than the 'simulation' and 'reference' RMs due to the beam convolution smoothing out the RM map to larger scales as seen in Fig. 8. For simulation Q6.5-D4-B1-S, the 'observable' RM structure function has an initial 'dip' at the lobe width scale, unlike the 'reference' and 'simulation' RMs. A similar departure from the power law is seen in the other four simulations too; however, it is most pronounced for the smaller magnetic field structures.

For the higher powered jet in simulation Q10.8-D1-B1, the 'simulation' and 'synthetic' structure functions are amplified above the 'reference' structure function. This indicates that the higher powered jet in the more dense environment can amplify the RM values above the 'reference' level more significantly than the jets in the higher density environment. We conclude that this is due to the greater compression and amplification in the Faraday screen (as discussed in Section 4.1), in agreement with the findings of Huarte-Espinosa et al. (2011b). However, for the dynamic range-limited 'observable' structure function, this amplification above the 'reference' level is lost. We see this also in simulation Q6.5-D4-B1-S. This highlights the importance of sensitivity in detecting the true underlying structure function associated with a source.

In Fig. 12, the 'shell width' grey vertical line (first from the left) corresponds to the length scale of the median projected path length through the Faraday screen. For the jets in the higher density environment, this length scale seems to be associated with the turnover for the 'observable' RM structure function; however, this may be coincident with the new projected lobe width after the dynamic range cut (see Fig. 8). This length scale does not seem to be associated with any particular feature of the structure functions in simulation Q10.8-D1-B1.

In general, the departure from power-law structure does not always result in a turn-down in the spectrum and depends on the structures of the cluster magnetic field and density profiles (e.g. Huarte-Espinosa et al. 2011b). However, since the magnetic field structures are the same in all simulations but Q6.5-D4-B1-S, the overall shape of the structure function is very similar (accounting for differences in jet shape). The decrease in central density can be seen in the decreased magnitude of the structure function for simulation Q10.8-D1-B1; likewise, the increased magnetic field can be seen for Q6.5-D4-B2. We note that the magnitude of the structure function does not seem to depend much on jet power, as there is little difference between the structure function magnitude for simulations Q6.5-D4-B1 and Q10.8-D4-B1. We also note that the smaller magnetic field structures in simulation Q6.5-D4-B1-

S do not seem to impact the magnitude of the structure function either.

In simulation Q6.5-D4-B2, the 'simulation' structure functions at the small-scale end are amplified above the 'reference' structure function. This is likely due to the central high-resolution grid patch influencing the evolution of the magnetic field, which occurs at higher ambient magnetic field strengths. This results in rapidly changing RM magnitudes on small scales, primarily along $y = 0$ and $z = 0$ (see Figs 7 and 8). These fluctuations occur on the smallest scale of the simulation grid, thus boosting the structure function at this end of the spectrum, even when interpolated to the coarser observing grid. We expect this effect to be purely numerical and not physically motivated.

5 DISCUSSION

5.1 Improvements and limitations of our methods

The methods presented in our paper extend previous works. We confirm the results of Huarte-Espinosa et al. (2011b) with higher resolution simulations. Using PRAiSE (Yates-Jones et al. 2022), we have made surface brightness images including full synchrotron, adiabatic, and inverse-Compton losses. We extend the RM analysis of Huarte-Espinosa et al. (2011a, b) and use a dynamic range threshold for these surface brightness images to create 'observable' spatial RM maps. We have considered the depolarization of our sources and the feasibility of observing these sources and their RMs to study AGN environments.

There are some drawbacks to our methods in this paper, primarily related to the modelling of the cluster magnetic field. The stretched grid in our simulations models the jets from pc to kpc scales well. However, the cluster magnetic field is generated on a uniform grid and then interpolated to this stretched grid. The non-uniform grid cells on the simulation grid influence the evolution of the magnetic field; this occurs on small scales in the high-resolution grid patches along the axes. This effect is most visible in the RM map for simulation Q6.5-D4-B2 (Fig. 4). As noted in Section 4.3.1, magnetic fields with shorter correlation lengths (higher minimum wavenumber) are more susceptible to magnetic diffusion on the stretched grid, and so this has limited our choice of magnetic fields to study here. We found that our simulated cluster magnetic fields (in all simulations but Q6.5-D4-B1-S), with their larger magnetic field correlation lengths, result in non-isotropic RMs in the RM maps. This indicates that the details of the magnetic field structure influence the RM properties. The key differences between our large- and small-scale magnetic fields are as follows:

(i) *RM FWHM:* The distribution of RM values is narrower for our shorter correlation length simulation (Q6.5-D4-B1-S), with a FWHM of 1176 ± 21 rad m^{-2} compared to 1478 ± 47 rad m^{-2}. This is due to the shorter correlation length magnetic field, which has more field reversals along each path length and smaller magnetic field structures in general, resulting in fewer extreme RM values.

(ii) *Laing-Garrington effect:* This effect is not seen as clearly for simulation Q6.5-D4-B1-S; however, for simulation Q6.5-D4-B1, it is a chance effect that depends on the orientation of the observer. The choice of the integration axis and direction has a greater effect on the resulting RM map for longer correlation length magnetic fields since there are fewer magnetic field reversals along each line of sight.

(iii) *Depolarization and measured RM FWHMs:* For the shorter correlation length simulation, the maximum and median depolarization frequencies are 1441 and 713 MHz, respectively, which is higher than the values for the longer correlation length simulation (1116 and 649 MHz, respectively). However, the frequency at which the 'true' FWHM of the RM distribution is still observable is lower for the shorter correlation length simulation (500 MHz compared to 800 MHz), as the depolarization frequency structures across the sources (Fig. 10) are different due to the smaller magnetic field structures.

(iv) *Structure functions:* Since the magnetic field structures are different in simulations Q6.5-D4-B1 and Q6.5-D4-B1-S, the shapes of the structure functions are different, though the magnitude is similar for all cases but the 'observable' case. For the shorter correlation length simulation, there is a greater reduction in magnitude for the 'observable' structure function, and it exhibits a clear local minimum at approximately 90 kpc, rather than a plateau as seen for simulation Q6.5-D4-B1.

Additionally, we note that the integration along the RM line of sight may result in numerical errors due to the nature of integrating a grid along an axis at some angle to the coordinate axes. We stress the importance of modelling the cluster magnetic field well and highlight this as an area for future improvements.

We also note that we have used a shock threshold corresponding to a Mach number $M \sim 1.18$. This is in contrast with the $M \sim 2.24$ threshold that is used in Yates-Jones et al. (2022), which corresponds to a critical Mach number above which particle acceleration is most likely to occur (Vink & Yamazaki 2014; Kang, Ryu & Ha 2019; Ha et al. 2022). This shock threshold changes the final luminosity of the source, which will in turn affect the size-luminosity tracks. We found that for the higher shock threshold, the size-luminosity track of the source in simulation Q10.8-D1-B1 was virtually unchanged; however, for the lower-powered jets, the size-luminosity tracks were reduced by ~ 20 per cent for total projected source lengths above $\sim$100 kpc. This reduction in luminosity is primarily due to a weaker shock in the hotspot region of these lower powered jets, resulting in less emission at the jet head. By using the lower shock threshold, the sources in simulations Q6.5-D4-B1, Q6.5-D4-B2, Q10.8-D4-B1, and Q6.5-D4-B1-S retain hotspot-like structures and therefore more closely resemble FR-II sources. The details of the particle acceleration are not critical to the results of this paper.

5.2 Implications for AGN jet feedback

The demonstrated ability of RM analysis to distinguish between different combinations of jet power and environment parameters has significant implications for the quantification of AGN jet feedback. This feedback is done in two ways for powerful FR-II jets: their bow shock heats the ICM and also lifts this gas out of the gravitational potential well (e.g. Alexander 2002; Hardcastle & Krause 2013, 2014). However, the effects of these mechanisms are impacted by the relationship between jet power and environment.

Despite very similar observable radio continuum features, the different jets in our simulations provide different amounts of feedback to the surrounding gas. As Table 2 shows, the jets in the higher density environment (simulations Q6.5-D4-B1, Q6.5-D4-B2, Q10.8-D4-B1, and Q6.5-D4-B1-S) sweep up and shock heat a larger mass of the surrounding gas: approximately 21 per cent of the gas within 150 kpc of the host galaxy for the denser environment, but only 9 per cent for the less dense environment. We cannot determine the difference in the amount of gas affected by feedback without information on the type of environment the source resides in.

Jets in less dense environments (simulation Q10.8-D1-B1) are more powerful for the same radio luminosity, and the resultant lobes

expand faster than in the low-power/high-density case (simulations Q6.5-D4-B1, Q6.5-D4-B2, and Q6.5-D4-B1-S). The high-power jet heats the shocked gas to higher temperatures (a median increase of 116 per cent, compared to a 21 per cent median increase for the lower power simulations), and is more effective in a less dense environment (in comparison, simulation Q10.8-D4-B1 has a 35 per cent increase in temperature). The shocked gas in simulation Q10.8-D1-B1 still has a lower density than the low-power jet simulations (Table 2). The combination of higher temperature and lower density results in much longer cooling times for the high-power jets, meaning more efficient negative feedback – albeit delivered to smaller masses of gas. This theoretical finding is consistent with the observational result that FR-II sources in groups provide longer-lasting feedback than cluster sources (Shabala et al. 2011).

These differences in the temperature and amount of gas affected by jet feedback cannot be distinguished using radio luminosity and size alone. As RM distributions can successfully distinguish between different environments, this approach may lead to more accurate estimates of AGN jet feedback.

6 CONCLUSIONS

In this paper, we presented three-dimensional relativistic MHD simulations of Cygnus A-like powerful radio galaxies in turbulent ambient magnetic fields. Using different combinations of jet and environment parameters, we present a solution to the degeneracy in the relationship between the size and luminosity of radio galaxies. By using Faraday rotation measures, we find that a higher environment density or a higher cluster magnetic field strength broadens the distribution of RM values in a given source, allowing jet environments to be characterized using the RM for the given density and magnetic field distributions.

By studying different combinations of jet and environment parameters, we also confirmed the findings of Huarte-Espinosa et al. (2011b) with higher resolution simulations. We found that the environment parameters have the greatest effect on the RM distributions, finding that both higher densities and stronger magnetic fields broaden the RM distributions and increase the range of RM values. Smaller magnetic field structures in the environment result in narrower RM distributions. For simulations with large magnetic field structures the jets act to align an underlying RM reversal with the jet axis. Similar structures are also seen in observations (Sebokolodi et al. 2020; Anderson et al. 2022). Our results stress the importance of modelling the external magnetic field accurately.

The effects of the environment on the FWHM of the RM distribution are visible in current and future surveys if the survey resolution is sufficient. We found that observing grid resolution better than 1 kpc (=0.889 arcsec at redshift z = 0.056075) is sufficient to model the RM distribution for our simulated sources. We apply a dynamic range threshold of 10 at 151 MHz to our RM maps. This threshold preferentially excludes information from the lobe edges (primarily in the equatorial region), where the jet enhances the RM the most. These thresholds used do not greatly affect the shape of the RM distribution, so any reasonable dynamic range should be sufficient to study similar Cygnus A-like sources. Current surveys such as POSSUM (Gaensler et al. 2010) and VLASS (Lacy et al. 2020) have sufficient RM resolution to sample RM distributions for sources similar to our simulated ones. For sources with insufficient surface brightness resolution, such as those at higher redshifts than our simulated sources, broad-band polarimetry has the potential to model the RM distributions (Anderson et al. 2016). Future surveys with SKA-low (Stepanov et al. 2008) and the ngVLA (Selina, Murphy & Beasley 2023) will have the capability to characterize AGN jet environments in more detail than current surveys.

The full RM maps discussed here are only visible for an observing frequency $\nu_{\rm obs} \gtrsim 1.5$ GHz. The maximum depolarization frequency ranges between 640 and 1579 MHz for our simulated sources. We found that the depolarization frequency decreases towards the jet axis and hotspots, indicating that the emission from recently shocked electrons in these regions will depolarize at a lower frequency. We measure the FWHM of the observable RM distribution for MHz frequencies, finding that the measurement becomes reliable at frequencies between 500−1000 MHz for our simulations. We found that a stronger cluster magnetic field strength results in depolarization at higher frequencies, and that higher powered jets in poor environments are more likely to be polarized at lower frequencies than sources in dense environments. We confirmed the result of Meenakshi et al. (2023) that larger magnetic field correlation lengths result in increased depolarization by the Faraday screen.

The structure functions of our RM maps follow the Kolmogorov power-law slope for scales smaller than the lobe width. After this point, the spectrum turns over, decreasing sharply at the lobe length scale. We found that our dynamic range threshold causes non-power-law behaviour at smaller length scales than the lobe width due to the removal of amplified RM values at the edges of the jet lobe. We also found that small numerical effects influenced the structure function of the high magnetic field simulation; this again stresses the importance of modelling the magnetic field well. Our simulations show that changes in the structure function of the lower powered jets can be primarily explained by the environment and shape of the jet cocoon (i.e. the 'RM window'), rather than the effects of source expansion on the environment. In contrast, the higher powered jet amplifies the RM structure function above the 'reference' ($t = 0$ Myr) level. This amplification is not seen when the dynamic range threshold is applied. We found also that the behaviour after the turnover at the lobe width scale is dependent on the details of the environment.

The differences between our simulations have implications for AGN feedback. We find that our high-powered jet in a low-density environment, with a narrow RM distribution, affects a lower percentage of environment gas, but it is more effective at increasing the temperature of and therefore changing the thermal state of the gas. Thus, combining Stokes I and Faraday rotation observations of radio galaxies opens a new window to studying AGN feedback in large surveys.

In this work, we have focused on using the RMs as a probe of environment. In future work, we will present synthetic observations using full Stokes' parameters to study the polarization properties of AGN jets. We will modify the synthetic emission code PRAiSE (Yates-Jones et al. 2022) to use the magnetic field in the jet cocoon to model our radiative losses and study the differences between the radio continuum properties of RMHD and RHD jets. This and future work will be used in the CosmoDRAGoN project (Yates-Jones et al. 2023) to study the synthetic emission of RMHD jets in realistic, magnetized, cluster environments.

ACKNOWLEDGEMENTS

The authors thank the reviewer for their insightful comments. LJ thanks the University of Tasmania for an Australian Government Research Training Program (RTP) Scholarship. PR thanks the University of Tasmania for the Don Gaffney Scholarship and the Gates Cambridge Trust for research funding. This research was carried out using the high-performance computing clusters provided by Digital Research Services, IT Services at the University of Tasmania. We

thank Knapen, Chamba & Black (2022) for their guide to writing astronomy papers. We acknowledge the support of the developers providing the PYTHON packages used in this paper: ASTROPY (Astropy Collaboration 2022), JUPYTERLAB (Kluyver et al. 2016), MATPLOTLIB (Hunter 2007), NUMPY (Harris et al. 2020), and SCIPY (Virtanen et al. 2020).

DATA AVAILABILITY

The data underlying this article will be shared on reasonable request to the corresponding author.

REFERENCES

Adebahr B. et al., 2022, A&A, 663, A103
Alexander P., 2002, MNRAS, 335, 610
Anderson C. S. et al., 2022, ApJ, 937, 45
Anderson C. S., Gaensler B. M., Feain I. J., 2016, ApJ, 825, 59
Asada K., Inoue M., Uchida Y., Kameno S., Fujisawa K., Iguchi S., Mutoh M., 2002, PASJ, 54, L39
Astropy Collaboration, 2022, ApJ, 935, 167
Baars J. W. M., Genzel R., Pauliny-Toth I. I. K., Witzel A., 1977, A&A, 61, 99
Boccardi B., Krichbaum T. P., Bach U., Mertens F., Ros E., Alef W., Zensus J. A., 2016, A&A, 585, A33
Boccardi B., Krichbaum T. P., Bach U., Ros E., Zensus A. J., 2014, in Proceedings of the 12th European VLBI Network Symposium and Users Meeting (EVN 2014). 7–10 October 2014., Proceedings of Science, Trieste, Italy. id.16
Burn B. J., 1966, MNRAS, 133, 67
Carilli C. L., Barthel P. D., 1996, A&AR, 7, 1
Carilli C. L., Perley R. A., Dreher J. W., Leahy J. P., 1991, ApJ, 383, 554
Carilli C. L., Taylor G. B., 2002, ARA&A, 40, 319
English W., Hardcastle M. J., Krause M. G. H., 2016, MNRAS, 461, 2025
Enßlin T. A., Vogt C., 2003, A&A, 401, 835
Fabian A. C., 2012, ARA&A, 50, 455
Fanaroff B. L., Riley J. M., 1974, MNRAS, 167, 31P
Ferriére K., West J. L., Jaffe T. R., 2021, MNRAS, 507, 4968
Gabuzda D. C., Nagle M., Roche N., 2018, A&A, 612, A67
Gaensler B. M., Landecker T. L., Taylor A. R., POSSUM Collaboration, 2010, BAAS, 42, 515
Gaibler V., Khochfar S., Krause M., Silk J., 2012, MNRAS, 425, 438
Gaibler V., Krause M., Camenzind M., 2009, MNRAS, 400, 1785
Garrington S. T., Leahy J. P., Conway R. G., Laing R. A., 1988, Nature, 331, 147
Granato G. L., De Zotti G., Silva L., Bressan A., Danese L., 2004, ApJ, 600, 580
Guidetti D., Laing R. A., Bridle A. H., Parma P., Gregorini L., 2011a, MNRAS, 413, 2525
Guidetti D., Laing R. A., Bridle A. H., Parma P., Gregorini L., 2011b, MNRAS, 413, 2525
Guidetti D., Laing R. A., Croston J. H., Bridle A. H., Parma P., 2012, MNRAS, 423, 1335
Ha J.-H., Ryu D., Kang H., Kim S., 2022, ApJ, 925, 88
Hardcastle M. J. et al., 2019, A&A, 622, A12
Hardcastle M. J., 2013, MNRAS, 433, 3364
Hardcastle M. J., Croston J. H., 2020, New Astron. Rev., 88, 101539
Hardcastle M. J., Krause M. G. H., 2013, MNRAS, 430, 174
Hardcastle M. J., Krause M. G. H., 2014, MNRAS, 443, 1482
Harris C. R. et al., 2020, Nature, 585, 357
Hovatta T., Lister M. L., Aller M. F., Aller H. D., Homan D. C., Kovalev Y. Y., Pushkarev A. B., Savolainen T., 2012, AJ, 144, 105
Hu Y., Stuardi C., Lazarian A., Brunetti G., Bonafede A., Ho K. W., 2024, Nature Communications, 15, 1006
Huarte-Espinosa M., Krause M., Alexander P., 2011a, MNRAS, 417, 382
Huarte-Espinosa M., Krause M., Alexander P., 2011b, MNRAS, 418, 1621
Hunter J. D., 2007, Comput. Sci. Eng., 9, 90
Hutschenreuter S. et al., 2022, A&A, 657, A43
Kaiser C. R., Alexander P., 1999, MNRAS, 305, 707
Kaiser C. R., Dennett-Thorpe J., Alexander P., 1997, MNRAS, 292, 723
Kang H., Ryu D., Ha J.-H., 2019, ApJ, 876, 79
Kluyver T. et al., 2016, in Positioning and Power in Academic Publishing: Players, Agents and Agendas IOS Press Amsterdam. p.87
Knapen J. H., Chamba N., Black D., 2022, Nat. Astron., 6, 1021
Krause M., Alexander P., Bolton R., 2007, From Planets to Dark Energy: the Modern Radio Universe, Proceedings of Science, Trieste, id.109
Lacy M. et al., 2020, PASP, 132, 035001
Laing R. A., 1988, Nature, 331, 149
Laing R. A., Bridle A. H., Parma P., Murgia M., 2008, MNRAS, 391, 521
Loi F. et al., 2019, MNRAS, 490, 4841
Manchester R. N., 1972, ApJ, 172, 43
Mandal A., Mukherjee D., Federrath C., Nesvadba N. P. H., Bicknell G. V., Wagner A. Y., Meenakshi M., 2021, MNRAS, 508, 4738
McKean J. P. et al., 2016, MNRAS, 463, 3143
McNamara B. R., Nulsen P. E. J., 2007, ARA&A, 45, 117
Meenakshi M., Mukherjee D., Bodo G., Rossi P., 2023, MNRAS, 526, 5418
Mignone A., Bodo G., Massaglia S., Matsakos T., Tesileanu O., Zanni C., Ferrari A., 2007, ApJS, 170, 228
Mignone A., Zanni C., Tzeferacos P., van Straalen B., Colella P., Bodo G., 2012, ApJS, 198, 7
Minter A. H., Spangler S. R., 1996, ApJ, 458, 194
Mukherjee D., Bodo G., Mignone A., Rossi P., Vaidya B., 2020, MNRAS, 499, 681
Murgia M., Govoni F., Feretti L., Giovannini G., Dallacasa D., Fanti R., Taylor G. B., Dolag K., 2004, ApJ, 424, 429
Nesvadba N. P. H. et al., 2021, A&A, 654, A8
O'Sullivan S. P., Lenc E., Anderson C. S., Gaensler B. M., Murphy T., 2018, MNRAS, 475, 4263
Owen F. N., Ledlow M. J., Morrison G. E., Hill J. M., 1997, ApJ, 488, L15
Powell K. G., 1997, in Hussaini M. Y., van Leer B., Van Rosendale J., eds, Upwind and High-Resolution Schemes. Springer, Berlin, Heidelberg, p. 570
Powell K. G., Roe P. L., Linde T. J., Gombosi T. I., De Zeeuw D. L., 1999, J. Comput. Phys., 154, 284
Pudritz R. E., Hardcastle M. J., Gabuzda D. C., 2012, Space Sci. Rev., 169, 27
Raouf M., Shabala S. S., Croton D. J., Khosroshahi H. G., Bernyk M., 2017, MNRAS, 471, 658
Raouf M., Silk J., Shabala S. S., Mamon G. A., Croton D. J., Khosroshahi H. G., Beckmann R. S., 2019, MNRAS, 486, 1509
Riseley C. J. et al., 2020, PASA, 37, e029
Roettiger K., Stone J. M., Burns J. O., 1999, ApJ, 518, 594
Sebokolodi M. L. L., Perley R., Eilek J., Carilli C., Smirnov O., Laing R., Greisen E. W., Wise M., 2020, ApJ, 903, 36
Selina R., Murphy E., Beasley A., 2023, BAAS, 55, id.357.02
Shabala S. S., Kaviraj S., Silk J., 2011, MNRAS, 413, 2815
Shimwell T. W. et al., 2022, A&A, 659, A1
Shklovskii I. S., 1963, Soviet Ast., 6, 465
Sijacki D., Springel V., Di Matteo T., Hernquist L., 2007, MNRAS, 380, 877
Simonetti J. H., Cordes J. M., Spangler S. R., 1984, ApJ, 284, 126
Snios B. et al., 2018, ApJ, 855, 71
Somerville R. S., Davé R., 2015, ARA&A, 53, 51
Steenbrugge K. C., Heywood I., Blundell K. M., 2010, MNRAS, 401, 67
Stepanov R., Arshakian T. G., Beck R., Frick P., Krause M., 2008, A&A, 480, 45
Takizawa M., 2008, ApJ, 687, 951
Turner R. J., Rogers J. G., Shabala S. S., Krause M. G. H., 2018, MNRAS, 473, 4179
Turner R. J., Shabala S. S., 2015, ApJ, 806, 59
Turner R. J., Shabala S. S., 2019, MNRAS, 486, 1225
Vaidya B., Mignone A., Bodo G., Rossi P., Massaglia S., 2018, ApJ, 865, 144
van Weeren R. J., de Gasperin F., Akamatsu H., Brüggen M., Feretti L., Kang H., Stroe A., Zandanel F., 2019, Space Sci. Rev., 215, 16

Vanderwoude S. et al., ., 2024, AJ, 167, 226
Vazza F., Brunetti G., Brüggen M., Bonafede A., 2018, MNRAS, 474, 1672
Vink J., Yamazaki R., 2014, ApJ, 780, 125
Virtanen P. et al., 2020, Nat. Methods, 17, 261
Vogelsberger M., Genel S., Sijacki D., Torrey P., Springel V., Hernquist L., 2013, MNRAS, 436, 3031
Yang H. Y. K., Reynolds C. S., 2016, ApJ, 829, 90
Yates P. M., Shabala S. S., Krause M. G. H., 2018, MNRAS, 480, 5286
Yates-Jones P. M., Shabala S. S., Krause M. G. H., 2021, MNRAS, 508, 5239
Yates-Jones P. M., Shabala S. S., Power C., Krause M. G. H., Hardcastle M. J., Mohd Noh Velastín E. A. N., Stewart G. S. C., 2023, PASA, 40, e014
Yates-Jones P. M., Turner R. J., Shabala S. S., Krause M. G. H., 2022, MNRAS, 511, 5225

This paper has been typeset from a TEX/LATEX file prepared by the author.